Ultra-High Energy Cosmic Rays and the study of Cosmic Magnetism

(Ultra-Hoch energetische kosmische Strahlung und die Erforschung kosmischen Magnetismus)

von
Stefan Hackstein
geboren am
12. Februar 1990

Bachelor-Arbeit im Studiengang Physik
Universität Hamburg

2014

1. Gutachter/in: Prof. Marcus Brüggen

2. Gutachter/in: Dr. Franco Vazza

Contents

1. Abstract

1.1. Abstract

Considerable effort is presently undertaken around the world to run experiments (e. g. EUSO, Auger) designed to determine the composition, the energy spectrum as well as the arrival directions of Ultra High Energy Cosmic Rays (UHECRs). The use of cosmological simulations is mandatory to interpret the observed data, for there is no simple way to predict propagation, which therefore has to be simulated by calculation.

This thesis focuses on studying the role of cosmic magnetic fields (CMF) in deflecting UHECRs by using cosmological numerical simulations to study the propagation of UHECRs in the Universe. Comparison of these results with upcoming measurements may shed light upon the origin of UHECRs and the magnetization of large-scale structures in the Universe.

1.2. Zusammenfassung

Derzeit wird in der ganzen Welt ein beträchtlicher Aufwand betrieben Observatorien zu bauen (z. B. EUSO, Auger), um mit deren Hilfe die Zusammensetzung, das energetische Spektrum sowie die Einfallsrichtung von Ultra Hoch Energetischer Kosmischer Strahlung (UHECRs) zu messen. Um die Messdaten zu interpretieren, bedarf es kosmologischer Simulationen zum Vergleich, da es keinen einfachen Weg gibt den Pfad der Teilchen zu prognostizieren.

Diese Dissertation beschäftigt sich mit der Rolle von kosmischen Magnetfeldern (CMF) bei der Ablenkung von UHECRs im Universum, indem deren Ausbreitung mittels verschiedener kosmischer numerischer Simulationen erforscht wird. Ein Vergleich dieser Daten mit kommenden Messungen kann für die Suche nach der Herkunft von UHECRs und der Magnetisierung von Großstrukturen im Universum hilfreich sein.

2. Introduction

The Earth is exposed to a permanent rain of particles from outer space, so called Cosmic Rays (CRs), whose first evidence was measured roughly 100 years ago by *T. Wulf* in 1909 and whose existence was first proposed by *V. Hess* in 1912 (*Hörandel* 2012 [**1**]). Since then big effort has been expended to figure out the nature of CRs. It was found that CRs consist of different kinds of particles that can reach very high energies above 10^{20} eV (*Letessier-Selvon* 2013 [**3**]), much larger than what can currently be achieved with terrestrial particle accelerators (e. g. LHC, fig. 2.1).

Low energy CRs ($E \lesssim 10^{15}$ eV) hit the ground and can be measured directly while above this threshold the CRs decay into showers of secondary particles (e. g. electrons, pions and muons) as they impact an atmosphere (*Auger* 1938 [**4**]). By measuring these products one can gather information on the energy and direction of arrival as well as on the composition of the primary particles, which is still not perfectly clear by now.
Particles that reach very high energies ($E \gtrsim 10^{15}$ eV) are the so called UHECRs (fig. 2.2). It is not yet known where these UHECRs originate neither how they are produced.

Preliminary findings suggest that the primary particles of CRs are mainly protons and alpha particles together with a small amount of fully ionized heavier nuclei. This amount changes with the energy of the primary particles (*Unger* 2013 [**5**]). Recent observations also indicate a transition above $E \gtrsim 10^{18}$ eV from isotropy to anisotropy that is in correlation to positions of Active Galactic Nuclei within the GZK horizon (*Santos* 2009 [**6**]).

2.1. Observatories

The observatories build to measure UHECRs (E $\gtrsim 10^{15}$ eV), e. g. the Pierre Auger Observatory in Argentinia, compose two types of detectors. The *Surface Detectors* form a large array of particle detectors, namely Cherenkov detectors, scintillators and muon detectors, to measure the secondary particles in the air shower that hit the ground. The energy density of different types of particles in the shower at ground level is used to derive the energy of the primary particles as well as to obtain knowledge on the composition.

The array is surrounded by *Fluorescence Detectors* that measure fluorescence light emitted by nitrogen molecules that were excited by secondary charged particles in air showers. By observing the longitudinal profile of energy of the shower one can measure the calorimetric energy of the primary particle and derive more information on its composition. The geometric structure of the shower can be determined by the arrival times of fluorescence photons together with the surface detections (fig. 2.3, *Necesal* 2010 [**7**], *Salamida* 2010 [**8**]).

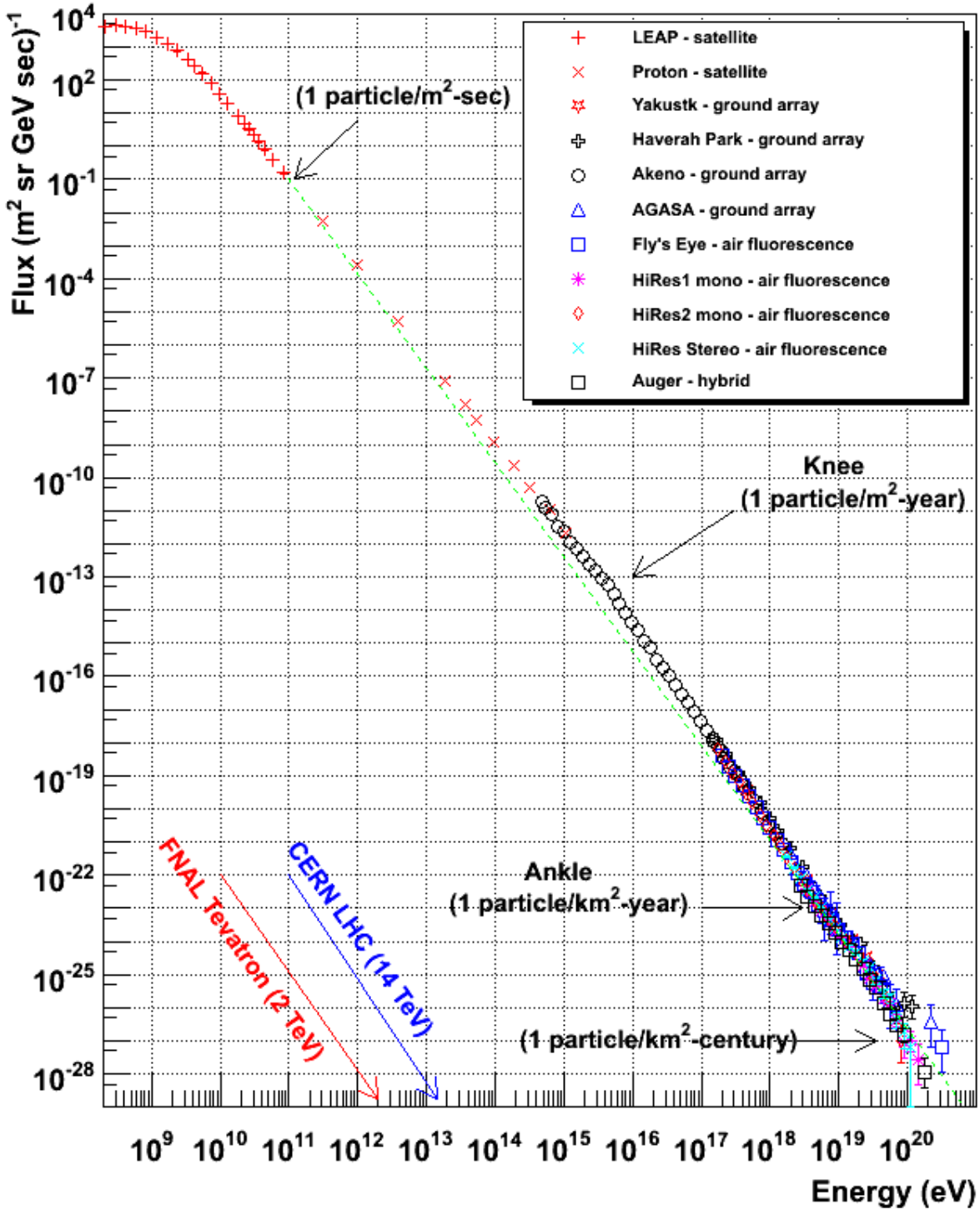

Figure 2.1: Arrival spectrum measurements of CRs as taken from various instruments (see label within the graph). (*Hanlon* [**2**]) The flux of CRs seems to follow a power law that changes power at the so called "knee" and "ankle". This indicates that there are different kinds of physical processes that take effect in the different energy regions.

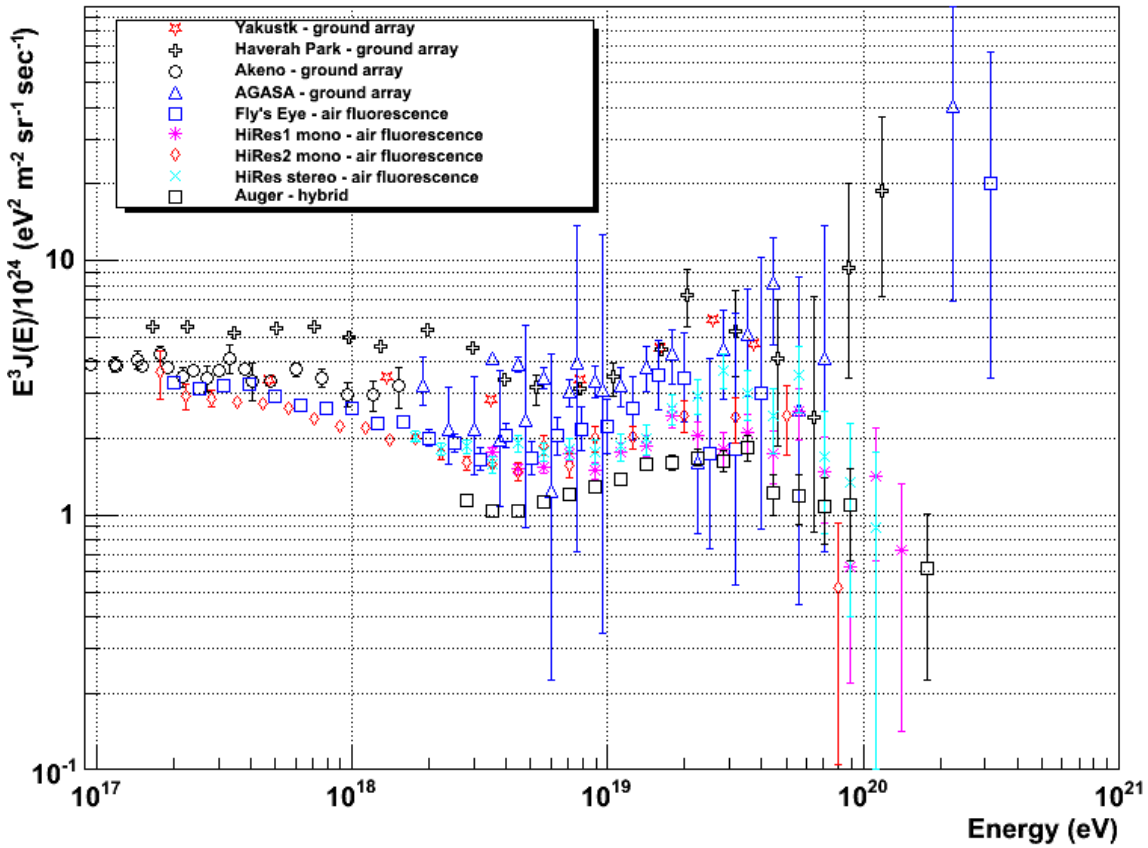

Figure 2.2: Arrival spectrum measurements of UHECRs as taken from various instruments (see label within the graph, *Hanlon* [**2**]). The spectra have been compensated by E^3 in order to better highlight the differences compared to the lower energy spectrum.

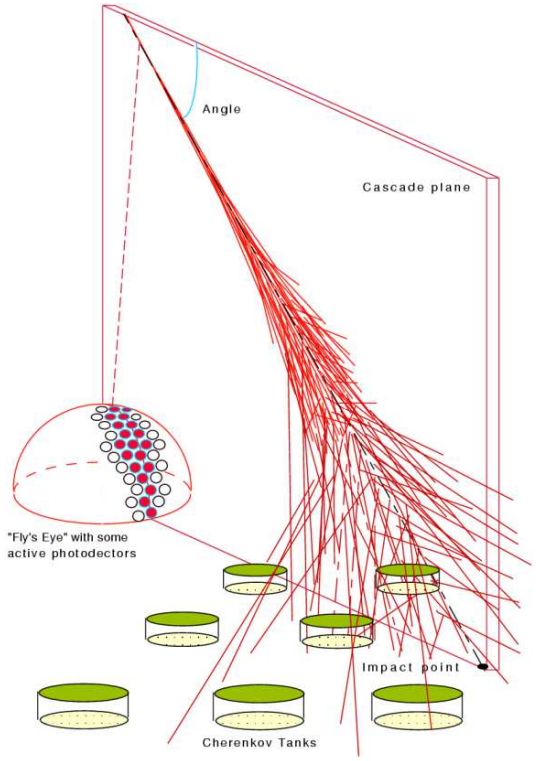

Figure 2.3: Cartoon of the hybrid detection technique . Charged particles at ground level are detected in surface detector stations while fluorescence light is collected in fluorescence detectors. (*Necesal* 2010 [**7**])

2.2. UHECRs processes

2.2.1. Deflection

To find out more about the origin of UHECRs it is crucial to know the physical mechanisms behind their propagation through the Universe. Since the CRs are moving charged particles, the primary mechanism that affects their propagation is the deflection by CMFs due to Lorentz force (in absence of electric fields):

$$\vec{F}_L = q\vec{v} \times \vec{B} \tag{2.1}$$

where q is the charge of the particle, $\vec{v}$ the velocity and $\vec{B}$ the magnetic field. Low energy CRs ($E < 10^{18}$ eV) in a CMF can be deflected to very large angles and are therefore confined by the magnetic field into their origin galaxy. This is predicted by the Larmor radius (e. g. *Sigl* 2001 [**9**]) which describes the radius of the spiral a charged particle would follow in a homogeneous magnetic field:

$$r_L = \frac{mv_\perp}{qB} \approx \left(\frac{E/Z}{\text{EeV}}\right)\left(\frac{B}{\mu\text{G}}\right)^{-1} \text{kpc} \tag{2.2}$$

where $v_\perp$ is the component of the velocity of the particle perpendicular to the direction of the magnetic field, q the particles charge, B the magnetic field strength, E is the Energy of the UHECR and Z its atomic number. For magnetic field strengths in order of B = 1 μG, which is common for galaxies and galaxy clusters (see Sec. 2.3), and an energy lower than E = 10^{18} eV this radius becomes $r_L \lesssim 1$ kpc, smaller than the common size of a galaxy thus resulting in the capture of the CRs at lower energies. Hence measured low energy CRs are likely to originate from within our own galaxy.
The higher the energy of the CRs, the lower is the deflection and thus the confinement. Therefore, the UHECRs are not confined within a galaxy and are likely originated elsewhere in the largest scales of the universe. Hence they are the only known measurable particles coming from outside our galaxy and are therefore crucial to better understand extragalactic physics.

2.2.2. Pair production

When propagating through interstellar space, UHECRs can interact with the ambient low energy photon fields, namely the cosmic microwave background (CMB) and the cosmic infrared background (IRB). This takes place as the process of pair production (known as the Bethe-Heitler process):

$$\gamma + p \rightarrow p + e^- + e^+$$

where γ is a photon, p is a proton, e^- is an electron and e^+ a positron. The different low energy photon fields due to their different energies are subject to different thresholds in this mechanism. The CMB contains but the lowest energy and as its threshold is about $6{\cdot}10^{16}$ eV (e. g. *Takami* 2012 [**10**]), far below the UHECRs we consider in this thesis, the CMB as well as the IRB contain enough energy to start this process at all times.

Though pair production has a short interaction length, it however causes relatively small energy losses.

2.2.3. Pion production and the GZK horizon

Another interaction with the CMB is the pion production via Delta resonance:

$$\gamma_{CMB} + p \rightarrow \Delta^{+} \rightarrow p + \pi^{0} \text{ or } n + \pi^{+}$$

where γ_{CMB} is a photon of the CMB, p is a proton, Δ^{+} is a Delta baryon, n is a neutron and π is a pion. The threshold for this reaction is the so called GZK limit $E_{GZK} \approx 5 \cdot 10^{19}$ eV (*Watson* 2013 [**11**]). The loss of energy caused by this effect is rather high so UHECRs can not travel too far distance above this limit. Measured high energy events therefore have to originate from within a sphere around the observer, whose radius is the so called GZK horizon of the order of 100 Mpc (*Watson* 2013 [**11**], *Greisen* 1966 [**12**], *Zatsepin, Kuzmin* 1966 [**13**]).

2.3. Cosmic magnetic fields

Recent measurements indicate that all galaxies and galaxy clusters contain magnetic fields and even the Intracluster Medium is permeated by them (e. g. *Brüggen* 2013 [**14**], *Bonafede* 2011 [**15**]). The evolution of CMF can not be observed directly, since the timespan of such processes is of cosmological order. Therefore, simulations have to be made to compare their outcome with the observations.

2.3.1. Origin of cosmic magnetism

At present there are several suggestions on the origin of CMFs that can reproduce the observed field strengths within galaxies and galaxy clusters. One is the existence of a primordial seed field with strength up to $10^{-4}\mu$G which has formed in the early universe and then amplified by turbulence and compression (e. g. *Widrow* 2011 [**16**]).
Another model states that CMF were caused by the charged outflow of galactic winds or active galactic nuclei of early galaxies ($z \lesssim 10$) that had generated magnetic fields of μG strengths. The early ejected wind bubbles contain field strengths in range of $10^{-2} - 10^{1}$ μG (*Bertone* 2006 [**17**], *Donnert* 2008 [**18**]). Other models, like the Biermann battery or generation of magnetic fields from plasma waves, are not taken into account in this thesis.

2.3.2. Observational evidences

To measure CMF one can use several effects. The most important effects to measure the fields of galaxy clusters are on one hand *Faraday rotation* and on the other *synchrotron emission*.

Faraday rotation
When electromagnetic radiation propagates through a magnetic field the plane of its polarization is rotated by

$$\Delta\theta \propto \lambda^2 n_e B_{||} dl \tag{2.3}$$

where λ is the wavelength of the radiation, n_e the number density of electrons, $B_{||}$ the magnetic field strength parallel to the direction of propagation of the radiation and dl the length of propagation (*Pudritz* 2012 [**19**]). Measuring the rotation of radiation on different wavelengths gives some indication of the magnetic field strength along the line of sight as well as of its direction, as the rotation angle is sensitive to the direction of the field. Faraday rotation is presently used to measure regular as well as highly tangled CMF (e. g. *Bonafede* 2010 [**20**]).

Synchrotron emission
As a charged particle is deflected radially by a magnetic field it emits polarized radiation. Most important for measuring CMF is the synchrotron radiation of relativistic electrons. These are present virtually everywhere in space and they deliver enough energy to produce radiation that can easily be measured, even over long distances. The intensity of the synchrotron radiation measured by the observer is

$$I \propto n_{e,rel} B_{\perp}^2 \tag{2.4}$$

where $B_{\perp}$ is the magnetic field strength perpendicular to the direction of propagation of the charged particle and $n_{e,rel}$ the number density of relativistic electrons (*Ginzburg & Syrovatskii* 1965 [**21**]). Along with the information about the density of electrons $n_{e,rel}$ one can measure the intensity I of the synchrotron radiation to derive the magnetic field strength $B_{\perp}$ (*Beck* 2008 [**22**]). The measured degree of polarization gives information about the degree of ordering of the magnetic field.

With these two effects together one can derive a 3D picture of CMF from radio waves.
It was found that the magnetic field strength in galaxy clusters is typically of the oder of 1 μG, but even higher fields up to 40 μG have been measured in cool cluster cores and in galaxies up to $z \sim 2$ (e. g. *Brüggen* 2013 [**14**]). In the Coma cluster it was found, that the average magnetic field strength over a volume of ~ 1 Mpc^3 is 2 μG. (*Bonafede* 2010 [**20**]).

3. Goals

This thesis will investigate the following issues:

- Observational signatures of isotropic vs. cluster based injection of UHECRs.
- Effects of the magnetic field seeding scenario on the arrival spectrum of UHECRs.
- Effects of the magnetic field seeding scenario on the anisotropy of arrival positions of UHECRs.

4. Main section

4.1. Simulations and Datasets

The simulations analyzed in this work have been produced with the grid code *ENZO* (The Enzo collaboration 2013), in the course of CHRONOS [1] (*The ENZO project* 2013 [**23**], call at CSCS, Lugano, Switzerland, with P.I. F. Vazza).

ENZO is a highly parallel code for cosmological magneto-hydro-dynamics (MHD), which uses a particle-mesh N-body method (PM) to follow the dynamics of the Dark Matter (DM) and a variety of shock-capturing Riemann solver to evolve the gas component.

The MHD simulations we present here employed the Dedner formulation of MHD equations (*Dedner* 2002 [**24**]) which uses hyperbolic divergence cleaning to preserve the Div(B) term identically equal to zero. The MHD solver adopted here uses the Piecewise Linear Method (PLM) reconstruction, where fluxes at cell interfaces are calculated using the local Lax-Friedrichs Riemann solver (*Kurganov & Tadmor* 2000 [**25**]) and time integration is performed using the total variation diminishing (TVD) second order Runge-Kutta (RK) scheme (*Shu & Osher* 1988 [**26**]). These simulations also made use of the recent porting on CUDA into the Dedner algorithm, in order to efficiently run on the GPU (*Wang & Abel* 2010 [**27**]). For the fixed grid simulations, like the one used here, we measured a speedup by a factor ~ 70 in the MHD section of the code, and by a factor ~ 4 for the full cosmological simulation.
In this work we studied different basic strategies to initialize the magnetic field at run time:

- simulation "*b10*" (256^3) and "*z0*" (512^3) (uniform early cosmological seeding): we initialize a uniform magnetic field with strength $B_0 = 10^{-4}\mu$G everywhere in the simulated volume at $z \sim 30$, and let cosmological structure formation to compress and amplify it;
- simulation "*b10_z1*" : similar to "*b10*", but we also assume a release of magnetic field from high density peaks in the 3D volume, which trace the distribution of galaxies and proto-clusters. At the injection epoch, each peaks releases an additional divergence free loop of magnetic field, whose strength is bound to be 50 percent of the r.m.s kinetic energy of the host cells. The injection epoch is fixed to $z \sim 1$. In general, the values of magnetic fields at the injection epochs are in the range of $\sim 10 - 50\mu G$;
- simulation "*b10_z2*" : similar to "*z1*" , but the injection epoch is $z \sim 2$ here;

Two simulations were used to first investigate the role of additional magnetic field seeding in the deflection of UHECRs. However, in the process of this thesis it was realized that the magnetization level of galaxy clusters is too high in this model (most likely due to coarse resolution

[1] Computationally-intensive, High-impact Research On Novel Outstanding Science)

effects, which do not fully enable the estimate of a proper r.m.s. kinetic energy here), and therefore in the following we will use these models only as a proxy to first identify the general trends related to galactic seeding of magnetic fields in 256^3 simulations.
In order to achieve more realistic simulated field strengths we resorted to newer simulations, which instead provide more realistic fields in clusters:

- simulation "*z0_z1*": similar to "*b10_z1*", but in this case the released extra magnetic energy is fixed to be 1 percent of the thermal gas energy within the host cells and is released only once at $z \sim 1$
- simulation "*z0_z2*": similar to "*b10_z2*", but also here the released extra magnetic energy is fixed to be 1 percent of the thermal gas energy within the host cells and is released only once at $z \sim 2$.

The reference volumes used in this work are comoving $(50\text{Mpc})^3$, which we simulated with a resolution of 256^3 (*b10*), and $(100\text{Mpc})^3$ with a resolution of 512^3 (*z0*). The size of the cells in each simulation is $\sim (200\text{ kpc})^3$.

Our simulations assume a "WMAP 7-year" cosmology with $\Omega_0 = 1.0$, $\Omega_B = 0.0455$, $\Omega_{DM} = 0.2265$, $\Omega_\Lambda = 0.728$, Hubble parameter $h = 0.702$, a normalization for the primordial density power spectrum $\sigma_8 = 0.81$ and a spectral index of $n_s = 0.961$ for the primordial spectrum of initial matter fluctuations, starting the simulations at $z_{\text{in}} = 30$ (*Komatsu* 2011 [**28**]).

4.2. Preliminary Analysis

The raw output of the ENZO simulations were analyzed with original algorithms written in IDL 7.1.1 (*IDL Software* [**29**]). A representative sample of these routines is given in the Appendix.

4.2.1. Maps

The maps in fig. 4.1 and 4.2 show slices of values of the *b10* simulations with a side length of 50 Mpc at the location of the most massive cluster (ID11). One can see, that the temperature and magnetic field is correlated with gas density as expected, because magnetic fields and temperature are increased during gas compression driven by gravity. The temperature of the gas is also strongly enhanced by shocks, while the magnetic field is amplified by chaotic motions, which develop in collapsed structures.

Fig. 4.2 shows the magnetic field of the simulations without (*b10*) and with additional magnetic field seeding at different cosmological redshift z (*b10_z1 & b10_z2*). One can see that the additional field adds up to the original magnetic field and then releases into the adjacent regions, resulting in a strong field that spread wider by $z \sim 0$. The central magnetic field is lower in case of an earlier release, while the volume occupied by significant values of magnetic field is increased in this case, since there was more time for advection motions to diffuse the seed fields. In the filaments this effect is also faintly present, but of such weak intensity that there are no significant changes. Outside of the clusters, far away from the peaks in the density, no effects can be recognized.

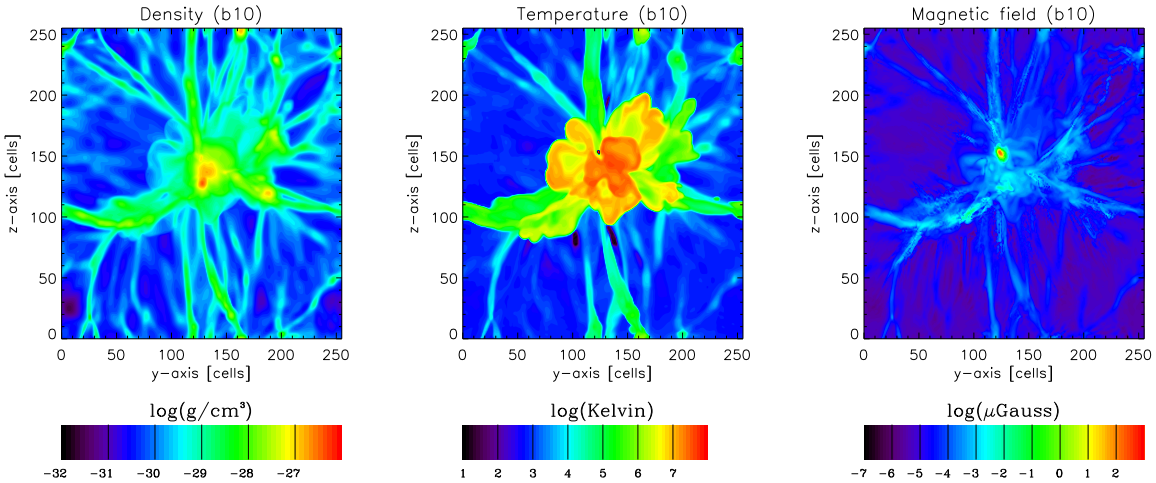

Figure 4.1: Maps of density, temperature and total magnetic field of *b10* simulation at $z \sim 0$. Shown are slices of one cell ($\sim$ 200 kpc) in x-y-plane of the most massive cluster (ID11) found in *b10*.

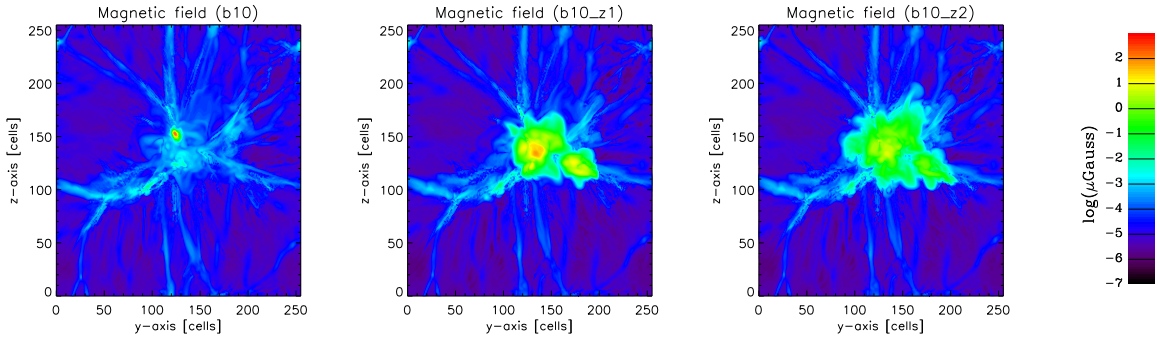

Figure 4.2: Maps of total magnetic field at $z \sim 0$ of *b10* simulation without and with additional magnetic field seeding at $z \sim 1$ (*b10_z1*) and $z \sim 2$ (*b10_z2*). Shown are slices of one cell ($\sim$ 200 kpc) in x-y-plane of the most massive cluster (ID11), which is the same for all *b10* simulations.

4.2.2. Volume Distributions

Fig 4.3 shows the amount of the volume that contains the given value of density or magnetic field respectively. While the density distribution is rather constant for all simulations, one can see that the magnetic field of the simulations with additional magnetic field seeding at $z \sim 1$ (*b10_z1*) and $z \sim 2$ (*b10_z2*) contain much more cells with higher values, but for *b10_z2* less than for *b10_z1*. This again shows that the additional magnetic field is simply added at density peaks and then releases into adjacent regions. One can also see that the magnetic field seeding cases of the 50 Mpc simulation (*b10_z1&z2*) results in too strong CMF ($B \gtrsim 10^2 \mu$G), so these simulations only give a qualitative trend. This situation is better for *z0_z1* and *z0_z2*, since they show CMF of observed strength ($B \sim 1 \mu$G, see sec. 2.3.2).

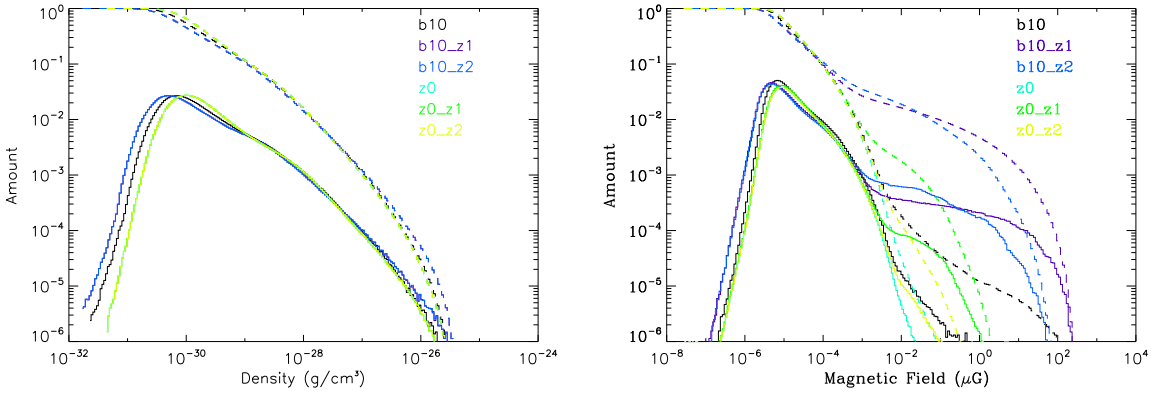

Figure 4.3: Distribution of density (left) and total magnetic field (right) in the cosmological volume for all examined simulations. The dashed lines show the cumulative, the solid lines the differential distributions.

4.2.3. Cluster Properties

Starting from the cluster positions and main parameters given from a halo finder run over the cosmological volume, we analyzed the cluster properties as a function of the assumed physical model. Here we only compare our simulations with very high magnetic field seeding, in order to have a clearer idea of the qualitative effects at play. In fig. 4.4 we show as an example the magnetic field of Cluster ID11 in the 50 Mpc *b10* simulations with a total mass enclosed within R200 (the radius enclosing 200 times the critical density of the Universe) of ~$4.5 \cdot 10^{13}$ $M_{\odot}$ and a temperature of ~$7 \cdot 10^{6}$ K.

In IDL we produce the profiles in fig. 4.5 by averaging the values of the cells at same distance from center (the code is given in A.2). It can be seen that the magnetic field is always maximum at the center of each cluster atmosphere and stays rather flat up to a distance of ~1 Mpc from the center.

Fig. 4.6 shows the relation between the maximum magnetic field strength and the maximum gas density within R200 of each cluster. This relation is rather flat for *b10* simulation, while instead for *b10_z1* and *b10_z2* the magnetic field seems to rise along with the density as expected, since denser halos would host more r.m.s. kinetic energy and hence more magnetic field is injected. In *b10_z1* the clusters always contain more magnetic field than in *b10_z2*, since by $z \sim 0$ the injected fields have been dispensed to larger radii in the second case. Together with the different environments of the clusters, that cause different amounts of additional magnetic field, this results in stronger scatter.

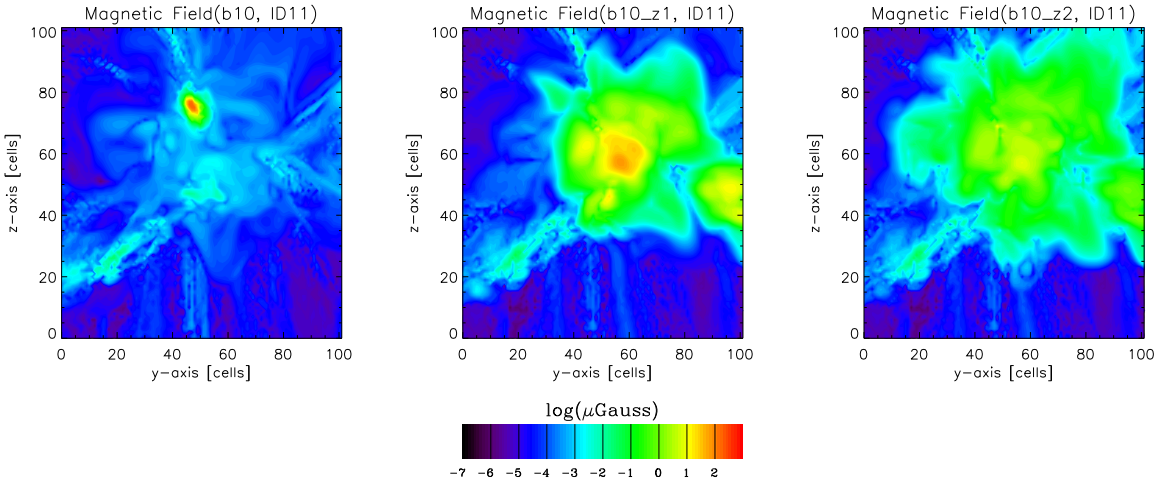

Figure 4.4: Color maps of magnetic field of Cluster ID11 at z=0 of the 50 Mpc simulations without (*b10*) and with additional magnetic field seeding at $z \sim 1$ (*b10_z1*) and $z \sim 2$ (*b10_z2*), the side of each panel is 20 Mpc, the slices are one cell ($\sim$ 200 kpc) thick.

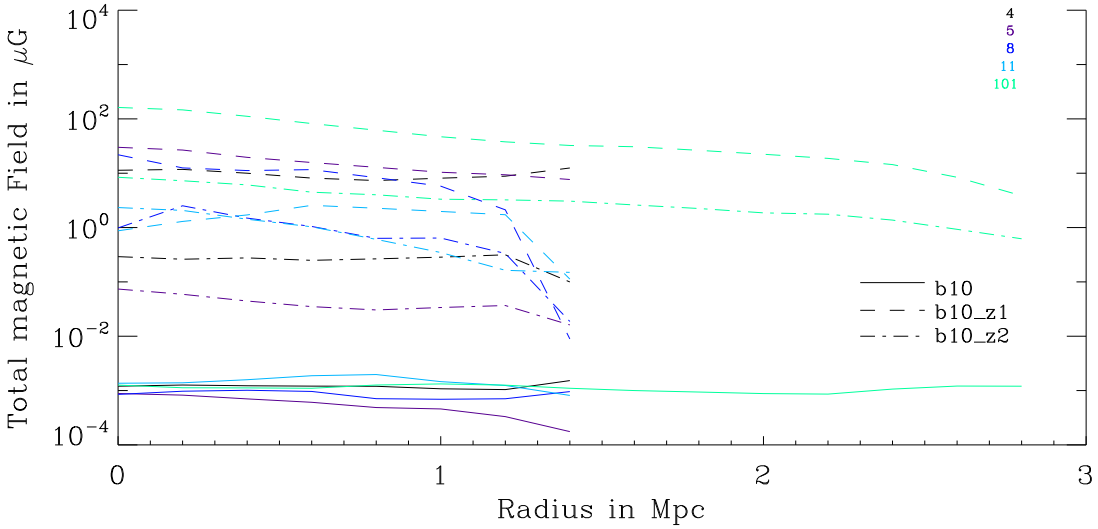

Figure 4.5: Profiles of total magnetic field for every cluster in simulations of the 50 Mpc simulations without (*b10*) and with additional magnetic field seeding at $z \sim 1$ (*b10_z1*) and $z \sim 2$ (*b10_z2*)

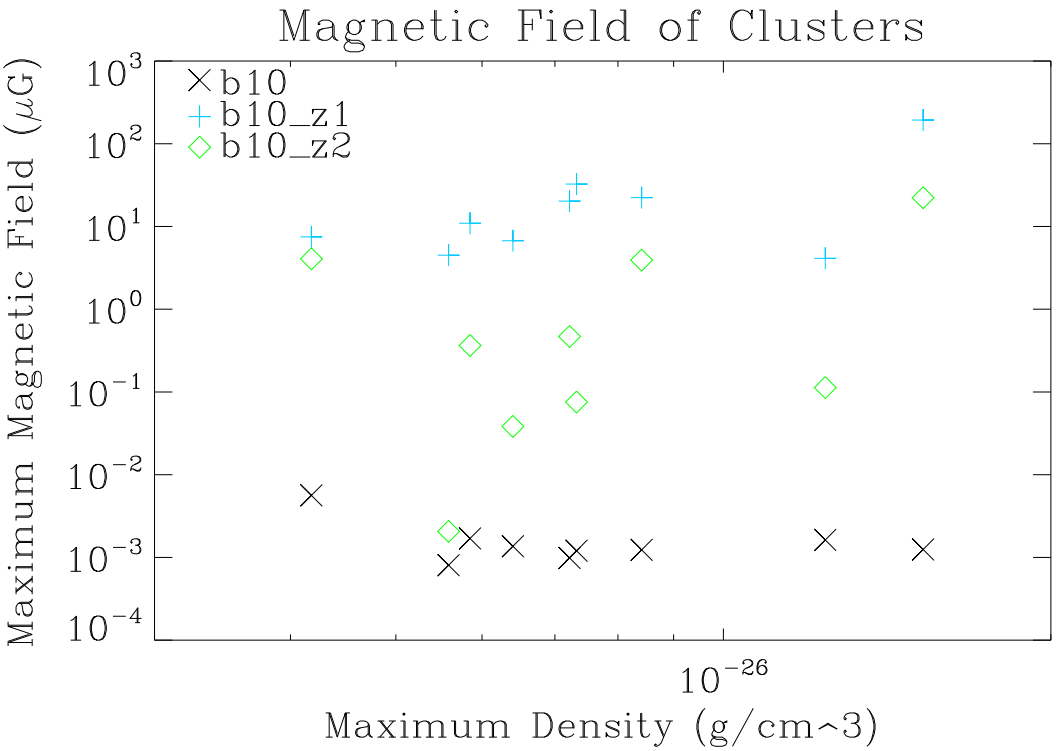

Figure 4.6: Scatterplot of magnetic field to density for every cluster in simulations of the 50 Mpc simulations without (*b10*) and with additional magnetic field seeding at $z \sim 1$ (*b10_z1*) and $z \sim 2$ (*b10_z2*) The density of the clusters stays the same for all simulations so the cells of the same density belong to the same cluster in different simulations

4.3. CRPropa

4.3.1. Basic Features of CRPropa

In this thesis we made use of CRPropa 3.0[2] (*Armengaud, Sigl* 2007[**30**], *Sigl* 2012 [**31**], *Alves Batista* 2013 [**32**]) which is a very powerful publicly available code to simulate the propagation of UHECRs in CMF. CRPropa works by injecting particles into a given 3D CMF simulation with some initial momentum, compute their propagation and energy losses until they hit an observer sphere, located somewhere in the simulation. The path of propagation is calculated step by step by integrating the Lorentz equations and computing interactions. Pair production (Sec. 2.2.2) is approached as a continuous energy loss, pion production (Sec. 2.2.3) by using SOPHIA[3], a Monte Carlo event generator designed to study this phenomenon (*Mucke* 2000 [**33**]). The size of the simulation box is limited so some particles may exceed the box in which they were injected, CRPropa then lets these particles continue their journey on the opposite side of this periodic box. The composition of the injected UHECRs can range up to an atomic number of $Z \leq 26$. The spectrum of injection can be defined choosing the range of energy and the input spectrum.
As a final output, CRPropa returns the position, momentum and energy of the initial and final state of all particles that hit the observer sphere as well as the distance they traveled.

The implemented physical effects are (see *Sigl* 2012 [**31**] for further explanation):

- *deflection*: The deflection of UHECRs in intergalactic magnetic fields due to Lorentz force (Eq. 2.1);
- *pion production*: By interacting with low energy photon backgrounds UHECRs can produce secondary mesons.
- *pair production*: The UHECRs can interact with the ambient low energy photon fields, by producing a pair of an elementary particle and its antiparticle;

In this thesis we only made use of single protons (Z=1), so photo-disintegration and nuclear decay, as well as many other features of CRPropa, are not taken into account here.

All runs with CRPropa were produced on Golem, a computing cluster owned by the University of Hamburg.[4]

[2] `https://crpropa.desy.de`
[3] Simulations Of Photo Hadronic Interactions in Astrophysics
[4] `www.hs.uni-hamburg.de/Golem`

4.3.2. Tuning of Parameters

CRPropa has several parameters that affect the output as well as the computation time. As a preliminary step in the use of CRPropa we performed extensive tests to calculate the optimal set of numerical/physical parameters for our given problem. The parameters we studied in course of this thesis are:

- `N`: Sets the total amount of injected particles;
- `min-/maxstep`: Defines the min-/maximum distance a particle may travel within one step of calculation;
- `Emin/-max`: Sets the min-/maximum Energy of injected particles;
- `observerSize`: Determines the radius of the observer sphere;
- `observerPosition`: Specifies the Position, where the center of the observer sphere is located;
- `Z`: Declares the atomic number of the injected particles;
- `Boxsize`: Predefines the size of the periodic box;

To find parameters that on one hand bring fast computation and on the other give correct physical results we made some preliminary tests on them in the 50 Mpc simulation (*b10*).
The default parameters for all runs in this preliminary tests were (unless stated otherwise):

```
minStep=500*kpc
maxStep=2.*Mpc
observerSize=5*Mpc
Emin=0.1*EeV
Emax=1000*EeV
Z=1
Boxsize=50*Mpc
```

The spectra for different amounts of injected UHECRs in fig. 4.7 shows, that the arrival spectrum is reasonably converged for an amount of 10^5 injected particles.

In fig. 4.8 it can be seen that smaller observer sizes need more computation time because there is a lower chance to hit a smaller sphere. Therefore the average distance increases with the computation time, because the particles need to pass more boxes before they hit the observer. Furthermore this affects the arrival spectrum, because the UHECRs coming from farer distances lose more energy. It would lead to more realistic results if the observer sphere was further decreased, but this would also make the computation time too large. We therefore chose `observerSize` = 4 Mpc as a best tradeoff between having a small enough observer and

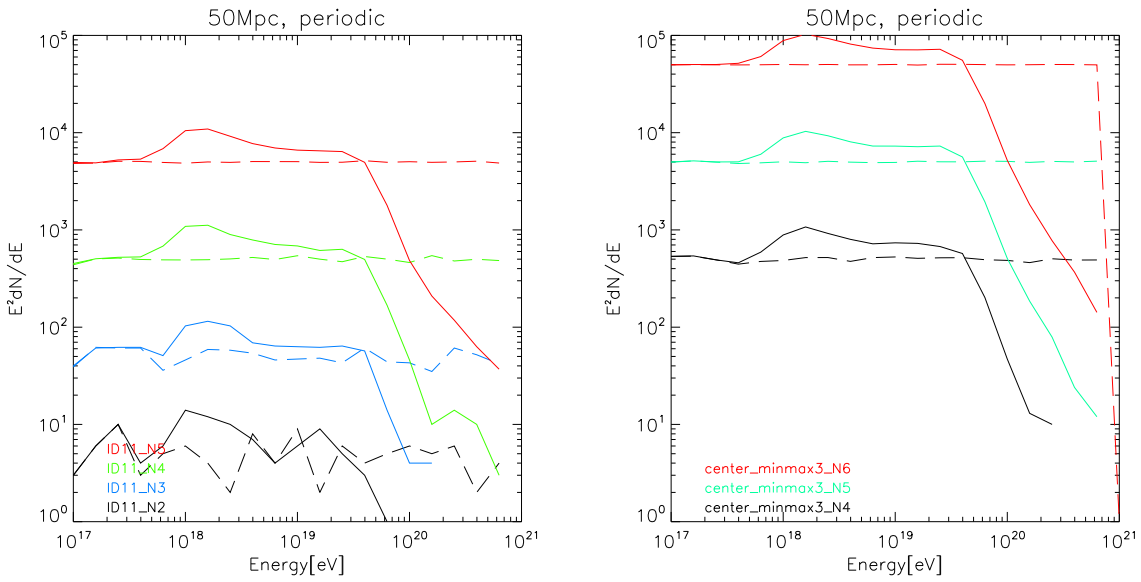

Figure 4.7: Spectra for changing the amount of injected particles, the dashed line is the initial, the solid line the final spectrum. The left panel shows spectra where the observer sits on cluster ID11, while in the right panel it is located in the center of the box and `min- and maxstep` is set to 3 Mpc. The number behind *N* shows the logarithmic magnitude of the total amount of injected particles.

limiting the computation time of each run.
One can also see there that changing the predefined boxsize does not affect the computation time too much in a wide range around the original size of the inserted simulation box. This anyway showed non physical results, most likely because the predefined box does not fit the inserted box, which is why the program uses a misshapen copy of the original simulation. So further on we set the predefined equal to the original boxsize.

The changes of `min- and maxstep` (fig. 4.9) do not show significant differences in the spectrum, but only in computation time. This at least as long as they remain in a suitable range below the distance to the next source or the size of the observer sphere. Therefore these parameters were set to `minstep` = 1 Mpc and `maxstep` = 3 Mpc so resulting in a short computation time but still with a sufficient range to vary in.

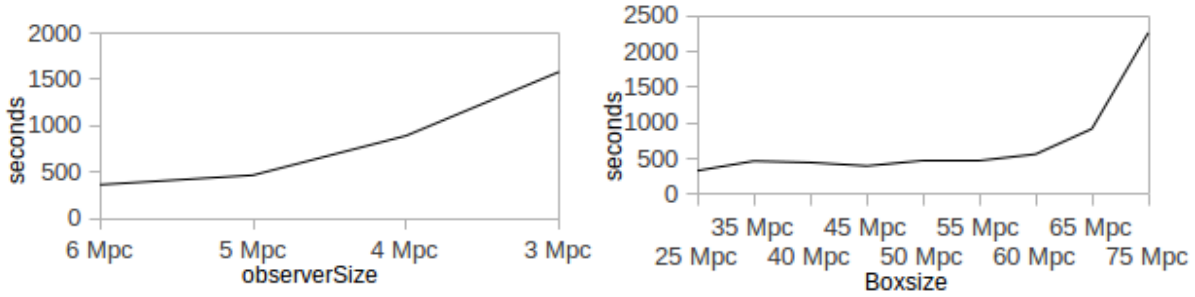

Figure 4.8: Total time in s taken for the calculation.

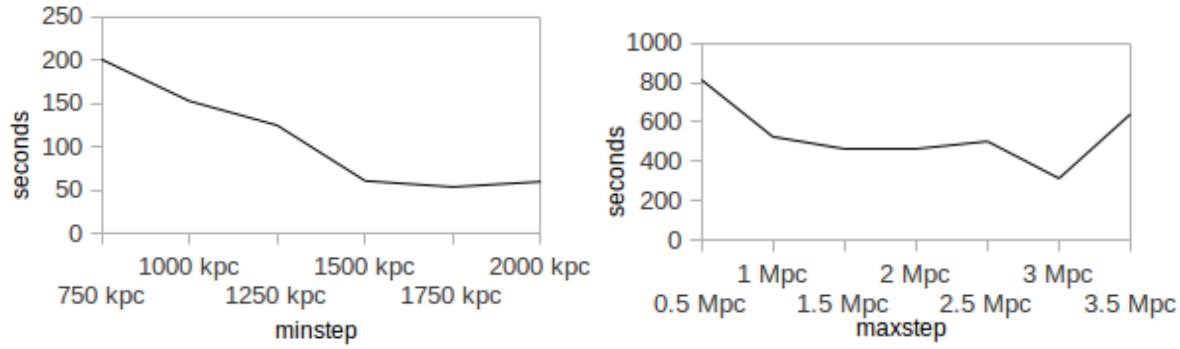

Figure 4.9: Total time in s taken for the calculation.

All the runs used to sound out the computation time were done once with 10^4 injected particles, so the total amount of time in seconds is always the same as the average time of calculation for one single particle in tenth of milliseconds, but do only show a rough trend. In detail, the `minimumEnergy` parameter was set to 0.1 EeV while the `maximumTrajectory` parameter was not set at all. They were held on those values for all *b10* runs. We found that changing these parameters would decrease the computation time without affecting the wanted results. We therefore set them to `minimumEnergy`: 10^{18} and 10^{19} eV, respectively, and `maximumTrajectory` = 4000 Mpc for the *z0* simulations.

4.3.3. Choice of suitable Parameters

In summary, our final choice of parameters for our production runs is as follows:

```
minStep=1.*Mpc
maxStep=3.*Mpc
observerSize=4*Mpc
Emin=1*EeV and 100*EeV, respectively
Emax=1000*EeV
Z=1
Boxsize=50*Mpc and 100*Mpc, respectively
```

Fig. 4.10 shows that the spectra for these parameters do not vary much for different clusters found in the same simulation.

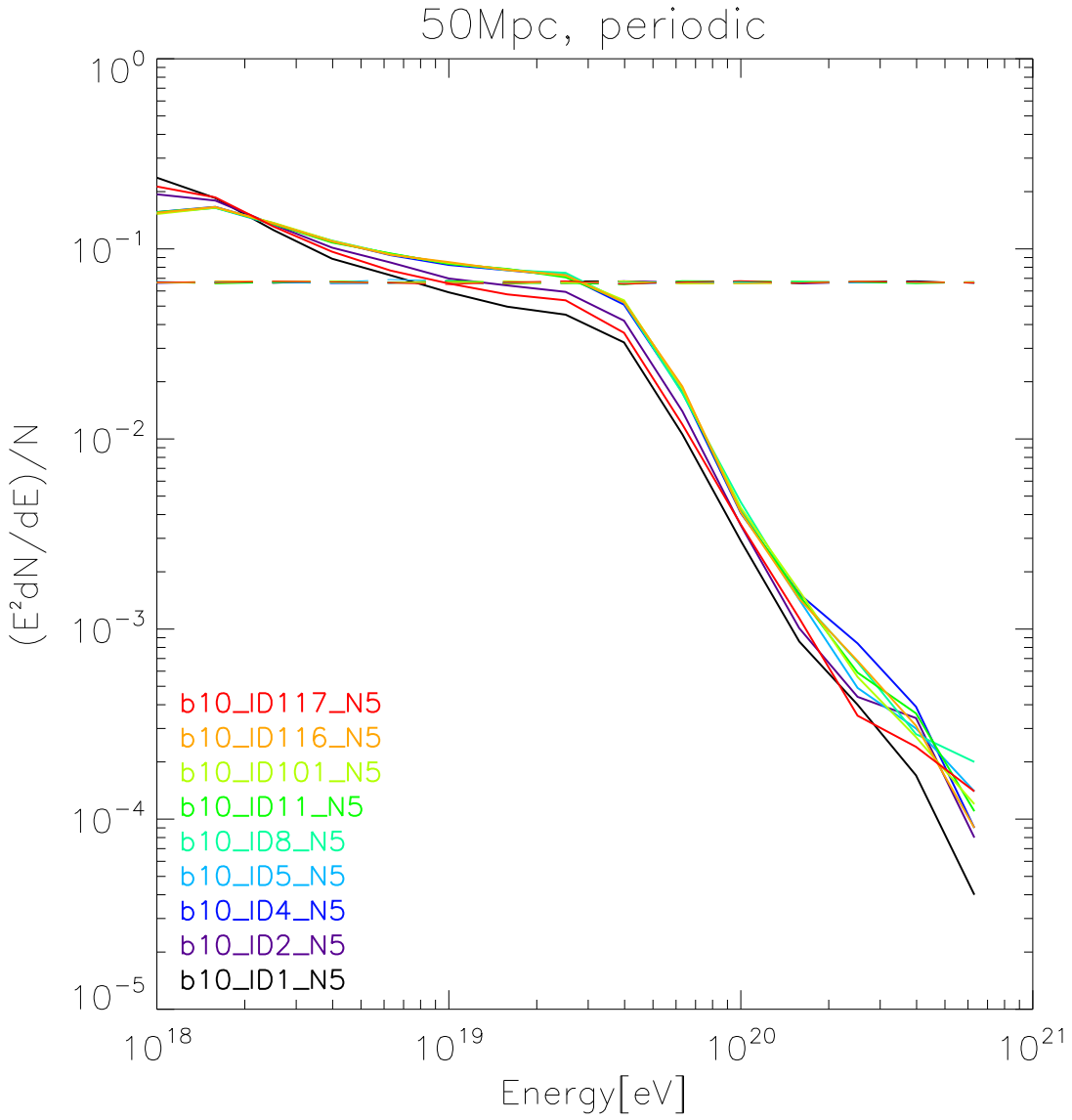

Figure 4.10: Spectra for observer located in different cluster positions, the dashed line is the initial, the solid line the final spectrum. For every run 10^5 UHECRs were injected.

5. Results and Discussion

5.1. Effects of Cluster Injection of UHECRs

In this section we will discuss the effects of injection of the UHECRs on their arrival spectrum and anisotropy, namely the difference between UHECRs injection on random positions vs. injection only from cluster centers. We therefore present the injection and arrival spectra (the code is given in A.3), as well as the cumulative anisotropic variance in number of UHECRs as a function of energy.
To calculate the anisotropic variance we first divide the equator of the current observer sphere in even parts with a fixed angular size ϕ in right ascension. We then count the number N of particles arriving in that parts with energy above the given limit. We name the mean deviation $\frac{\Delta N}{\langle N \rangle}$ for every part the anisotropy profile (e. g. fig. 5.5, the code is given in A.4). The anisotropic variance σ_N is the standard deviation of those values (the code is given in A.5):

$$\text{Anisotropic variance } \sigma_N = \sqrt{\left\langle \left(\frac{\Delta N}{\langle N \rangle} \right)^2 \right\rangle - \left\langle \frac{\Delta N}{\langle N \rangle} \right\rangle^2} \tag{5.1}$$

In order to have a Poissonian shot noise $\frac{\sqrt{N}}{N} \leq 10\%$, depending on how many particles N end up in a sector of ϕ, we fix the angular size accordingly. We chose $\phi = 5^\circ$ to obtain a good balance between resolution and Poissonian shot noise. Finally we take the average of σ_N over several CRPropa runs in the same MHD simulation, where the observer sphere with radius of 5 Mpc is placed on different cluster center positions.
We used σ_N to easily compare the anisotropy and its dependence on the arrival energy of UHECRs. We comment that although the production of all-sky maps of events and the decomposition of the observation of UHECRs into spherical harmonics would have had more direct application to real observations, in this thesis we resorted to this faster statistical approximation for the sake of simplicity.

In fig. 5.1 one can see that the mean anisotropic variance for random injection is nearly the same as the Poissonian shot noise within the sample and therefore probably mainly caused by statistics, although the standard deviation is very small. For cluster injection there are more UHECRs arriving with over 10^{20} eV, thus there is a lower shot noise. One can see an excess of anisotropy for $E > 10^{19}$ eV compared to the shot noise.

In fig. 5.2 one can see as an example cluster ID118 of the 100 Mpc simulation (*z0*) with the departure and arrival position and momentum of UHECRs in a cluster injected run. It shows that the UHECRs arriving with more than 10^{20} eV (red arrows) do all emerge from within a "small" sphere ($r \lesssim 100$Mpc) around the observer, while the UHECRs in the lower

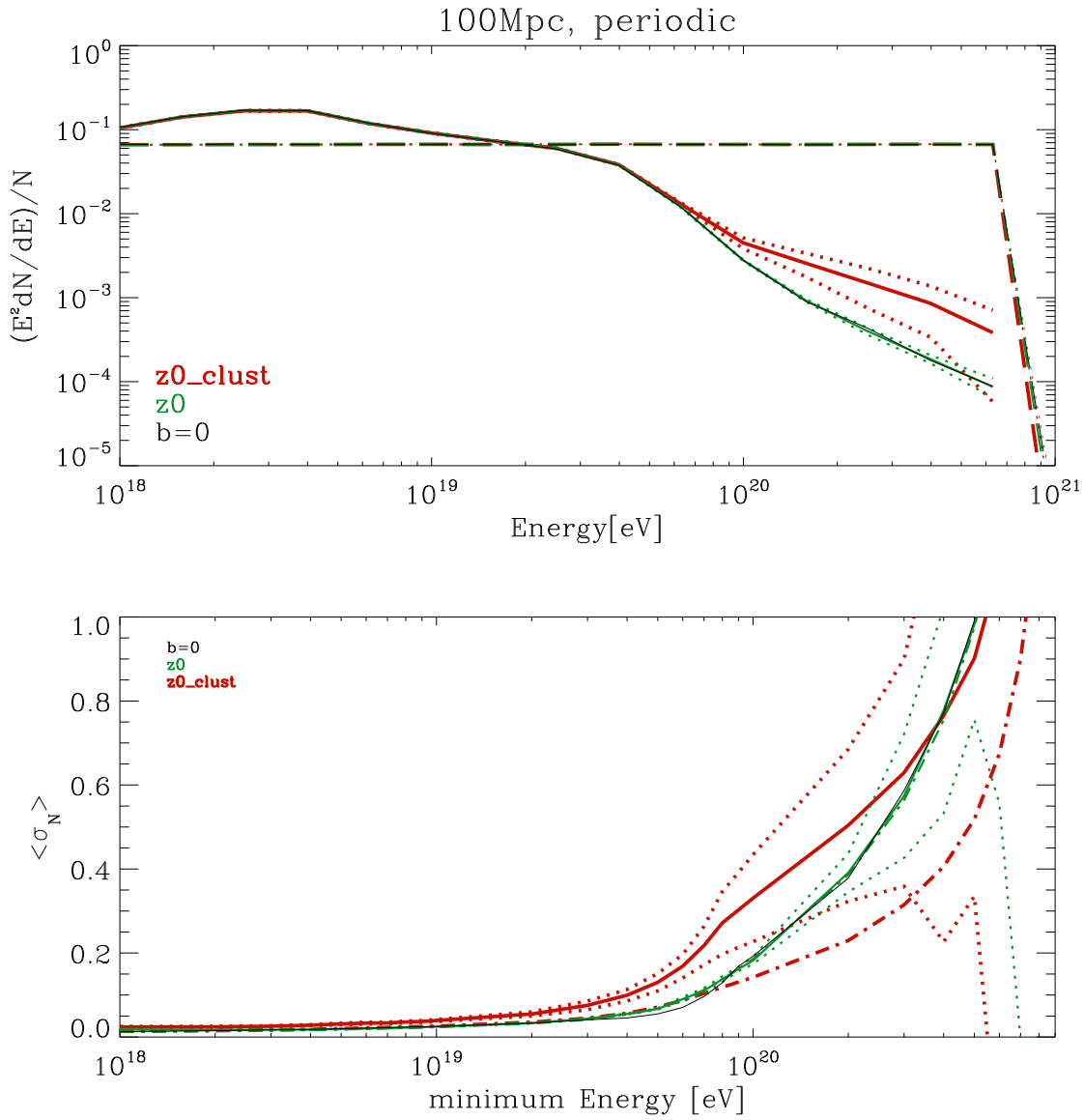

Figure 5.1: Spectrum (top) and anisotropic variance σ_N (bottom) of the 100 Mpc simulation for random (*z0*) and for cluster injection (*z0_clust*). This figure shows the average of 5 clusters for 10^7 injected UHECRs. The dashed line shows the injected spectrum, the solid line the arrival spectrum. The dotted lines show the corresponding 2σ standard deviation. The dash dotted lines show the mean Poissonian shot noise. The *b=0* case is a single random injection run without magnetic fields for comparison.

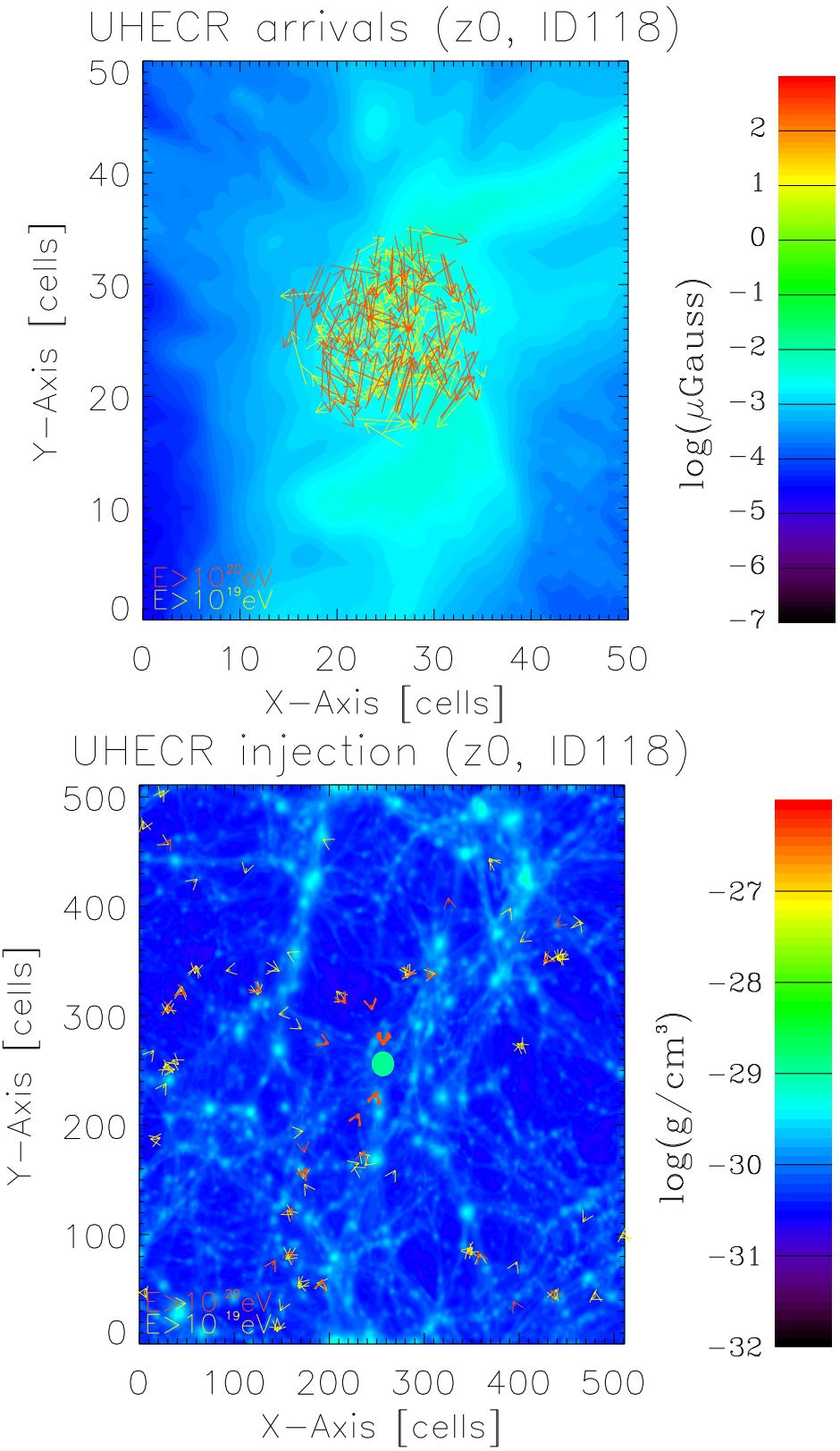

Figure 5.2: Local magnetic field (top) of Cluster ID118 as an average over the cluster (diameter of 4 Mpc) and mean density (bottom) of the whole 100 Mpc simulation (*z0*) with the arrows of momentum and position for arrival and injection. The cyan sphere in the middle of the injection map shows the observer. The thickness of the arrows indicates the distance that the corresponding UHECR has traveled, the more times it needed to pass the periodical box to hit the observer, the thinner the arrow is. None of the red arrows lost thickness, therefore they all had to emerge within one boxsize of 100 Mpc which equals the length of 512 cells.

energy ranges may also have traveled longer distances. This is due to the pion production which rapidly reduces the energy of particles above the GZK limit $5{\cdot}10^{19}$ eV so restricting the maximum travel distance of those UHECRs.
The local environment therefore has a strong effect in that energy range. This is on the one hand the effect of the amount of UHECR producing clusters within the GZK sphere on the spectrum, which statistically changes the fraction of UHECRs arriving with energies above the GZK limit. On the other hand there are only a few clusters within the GZK sphere on which those UHECRs were injected. At such high energies the deflection is very low (see Eq. 2.2), so the UHECRs may hardly be scattered homogeneously among the sky of the observer thus resulting in stronger anisotropy than the random injection.

To gain better statistics for the higher energy ranges in affordable computation time we restricted the injection energies to $10^{20} - 10^{21}$ eV and forced CRPropa to only evolve particles above 10^{19} eV. In fig. 5.3 one can see again $\langle \sigma_N \rangle$ is the same as the Poissonian shot noise for random injection, but for cluster injection one can see an excess of anisotropy for $E > 10^{19}$ eV compared to the shot noise, but not more than at 2 sigma level for all models. This confirms that, at sufficiently large energies, we do observe a significantly enhanced anisotropy of events at the observer, if UHECRs are released from galaxy clusters instead than in a random isotropic way.

Despite the fact that our method for estimating the anisotropy of arrival directions is obviously simplistic, compared to the current modelling of real UHECRs data with spherical harmonics (e. g. *Sommers* 2000 [**34**]), we found a remarkable similar trend (also at the quantitative level) with real data of Agasa (*Deligny* 2012 [**35**]). They reported values of the anisotropy consistent with our ones: $\sim 1\%$ at 10^{18}eV and $\sim 50 - 100\%$ for $\geq 10^{20}$eV. Similar to our case, they also conclude however that most of the high-energy anisotropy is consistent with statistical noise within the error bars.

Summary 5.1:

- The injection of UHECRs from clusters can be distinguished from random isotropic injection for $E > 10^{20}$ eV events, as the arrival spectrum is higher by a factor of ~ 2.
- The anisotropy as a function of energy shows detectable differences between random and cluster injection for $E > 5 \cdot 10^{19}$ eV. While in the case of random isotropic injection the anisotropy is consistent with the Poissonian noise statistics, in the cluster injection case the absolute anisotropy is significantly larger (even if only on the $1 - 2\sigma$ level) than the Poissonian shot noise at high energy.

Both results are stable against the increase of the number of events at high energy. Future runs with $10^7 - 10^8$ CRs injected at $E > 10^{20}$ eV will be necessary to further reduce the Poissonian shot noise and pin down physical effects in this regime.

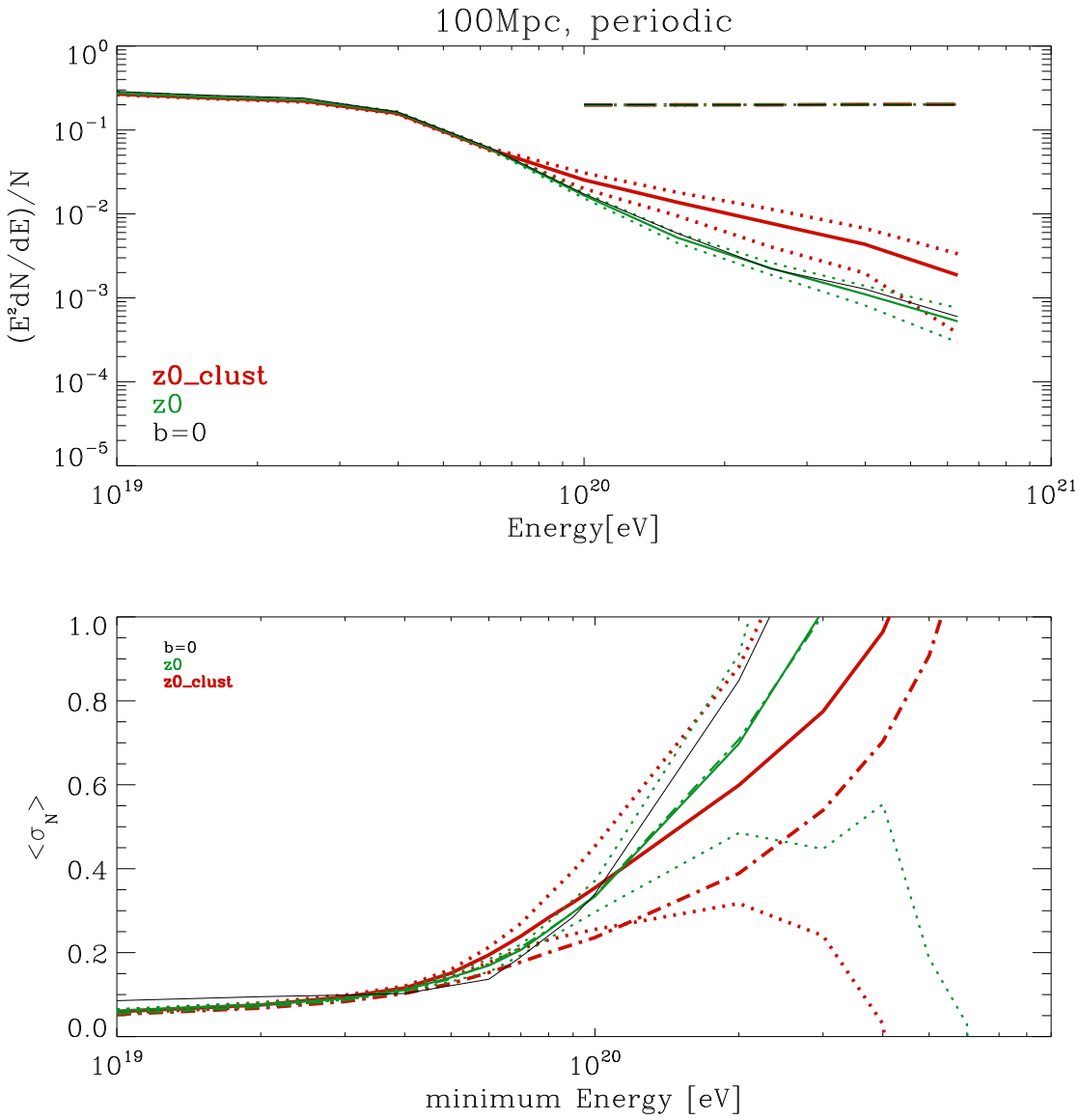

Figure 5.3: Spectrum (top) and anisotropic variance σ_N (bottom) of the 100 Mpc simulation for random (*z0*) and for cluster injection (*z0_clust*). This figure shows the average of 10 clusters for 10^6 injected UHECRs where the energy range of injection is limited to the range of 10^{20} to 10^{21} eV and only UHECRs with arrival energy above 10^{19} eV are considered. The dashed line shows the injected spectrum, the solid line the arrival spectrum. The dotted lines show the corresponding 2σ standard deviation. The dash dotted lines show the mean Poissonian shot noise. The *b=0* case is a single random injection run without magnetic fields for comparison.

5.2. Effects of magnetic field seeding scenarios

In this section we will examine the effects of the different magnetic field seeding scenarios. We again present the injection and arrival spectra (the code is given in A.3), as well as the average cumulative anisotropic variance as a function of energy, which describes the standard deviation of the anisotropy profiles (e. g. fig. 5.5, the code is given in A.4 and A.5).

5.2.1. 256^3 box

At first we will discuss the different seeding models of the *b10* simulation, examined with random injection only. Those simulations resulted in too strong cluster magnetic field strengths by a factor of roughly 100, so this only gives a qualitative trend to guide our following interpretation, since trends will be exaggerated here.

Fig. 5.4 shows that the seeding model does not play a relevant effect on the arrival spectrum of the UHECRs but it seems to affect the anisotropy at lower energy, where it gets larger than the shot noise. The simulation without additional magnetic field seeding (*b10*) shows no difference from the model without magnetic field (*b=0*). This indicates that the magnetic field makes little effect on the propagation of UHECRs in the very high energy region, while the effect is significant at lower energies. This follows from the prediction of the Larmor radius $r_L \propto \frac{E}{B}$ (2.2) that results in lower deflection for higher energies, thus less dependence of their anisotropy profile on the local magnetic field environment, unless there are very strong magnetic field strengths nearby.

Fig. 5.5 shows that only a few cluster anisotropy profiles are affected by the changes in the magnetic field caused by additional field seeding. This is due to their massive local environment, which results into seeding from many objects within a small volume (see fig. 4.4, which shows the extreme case of ID11).
As the *b10* runs have a far too strong magnetic field seeding it was crucial to confirm the results with a more realistic simulation, as in the following section.

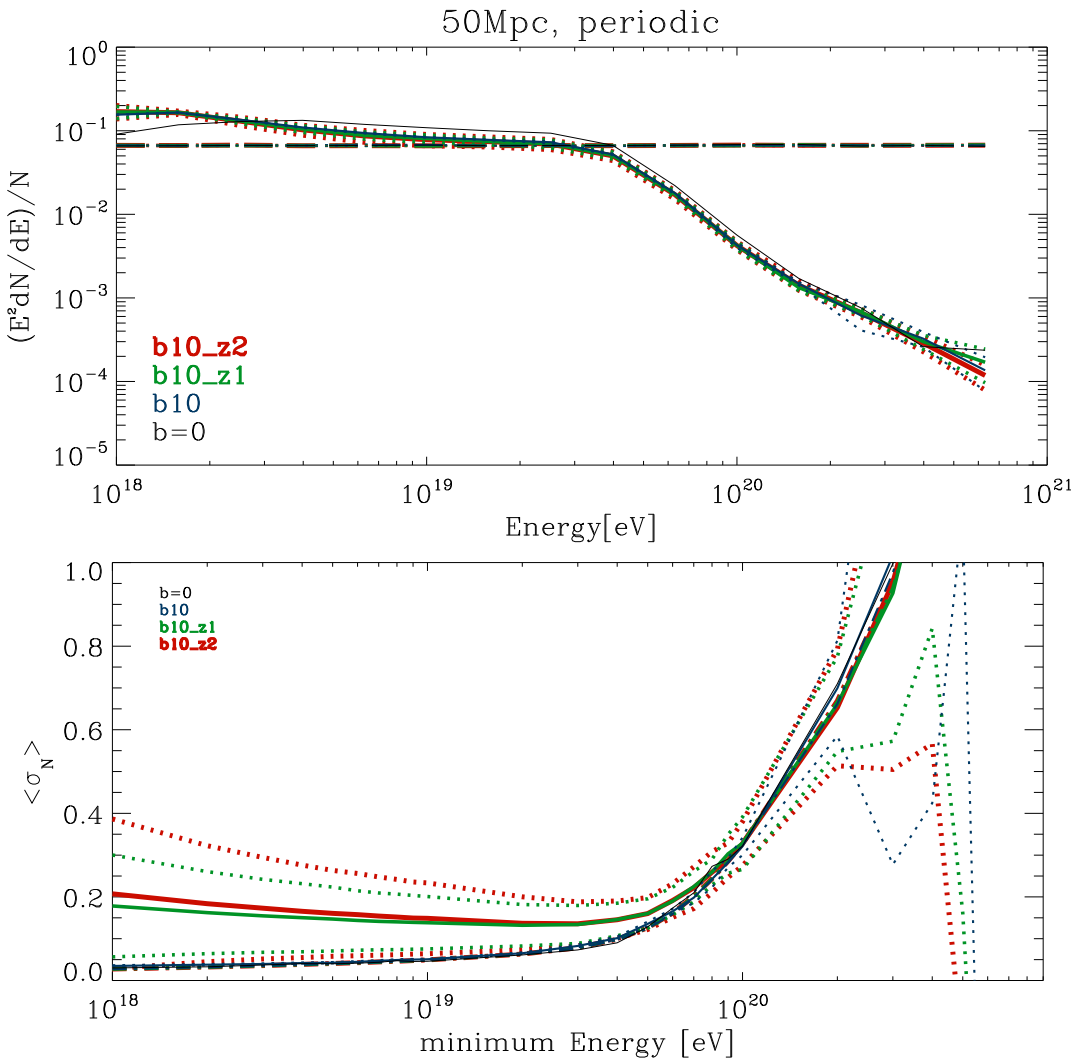

Figure 5.4: Spectrum (top) and anisotropic variance σ_N (bottom) of the different seeding models of the 50 Mpc simulations without (*b10*) and with additional magnetic seeding at $z \sim 1$ (*b10_z1*) and $z \sim 2$ (*b10_z2*) for random injection. This figure shows the average of 5 clusters for 10^5 injected UHECRs. The dashed line shows the injected spectrum, the solid line the arrival spectrum. The dotted lines show the corresponding 2σ standard deviation. The dash dotted lines show the mean Poissonian shot noise. The *b=0* case is a single random injection run without magnetic fields for comparison.

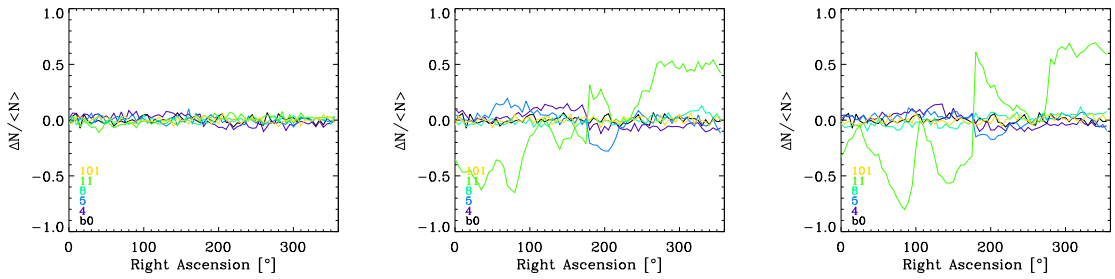

Figure 5.5: Anisotropy profiles of arriving UHECRs of the 5 different clusters in 50 Mpc simulations without (*b10*) and with additional magnetic seeding at $z \sim 1$ (*b10_z1*) and $z \sim 2$ (*b10_z2*). Shown is the variation of number of particles arriving within 5° of right ascension. In each panel we also show the anisotropy for one observer in the $b = 0$ model, that by definition gives the level of the Poissonian shot noise in the runs.

5.2.2. 512^3 box

To confirm the findings in the previous section we examined the different seeding models of the 100 Mpc simulation (*z0*) using cluster injection of UHECRs. This simulations show cluster magnetic fields of the order of $\sim 1\mu$G, of the order of what is suggested by observations, and are therefore more realistic than the *b10* ones.

Fig. 5.6 shows generally the same trends already discussed in the previous section but the anisotropy in the lower energy range exceeds the shot noise only for the *z0_z1* simulation (with additional magnetic field seeding on density peaks at $z \sim 1$). The effect may be provoked by the massive local environment that seeds strong magnetic fields from many nearby objects. As fig. 5.7 of Cluster ID490 of the 100 Mpc *z0* simulations shows, this additional seeding first strengthens the magnetic field of the dense cluster cores and then releases into the adjacent regions. More precisely, the additional magnetic field seeding at $z \sim 1$ did not have as much time for releasing large magnetic fields into large volumes as the other simulation with seeding at $z \sim 2$, so resulting in stronger magnetic fields in first case. Fig. 5.8 shows that the presented cluster shows the largest amount of anisotropy.

In order to gain more statistics in the higher energy regions in affordable computation time, we again restricted the injection energies to $10^{20} - 10^{21}$ eV and only considered particles above 10^{19} eV in the compilation of output events.
Fig. 5.9 confirms that for the energies above 10^{19} eV the effect of the seeding model is present, but also compatible with the Poissonian shot noise at the 2σ level. Therefore, no conclusive evidence about the impact of seeding on the observed anisotropy of UHECRs can be drawn from these data.

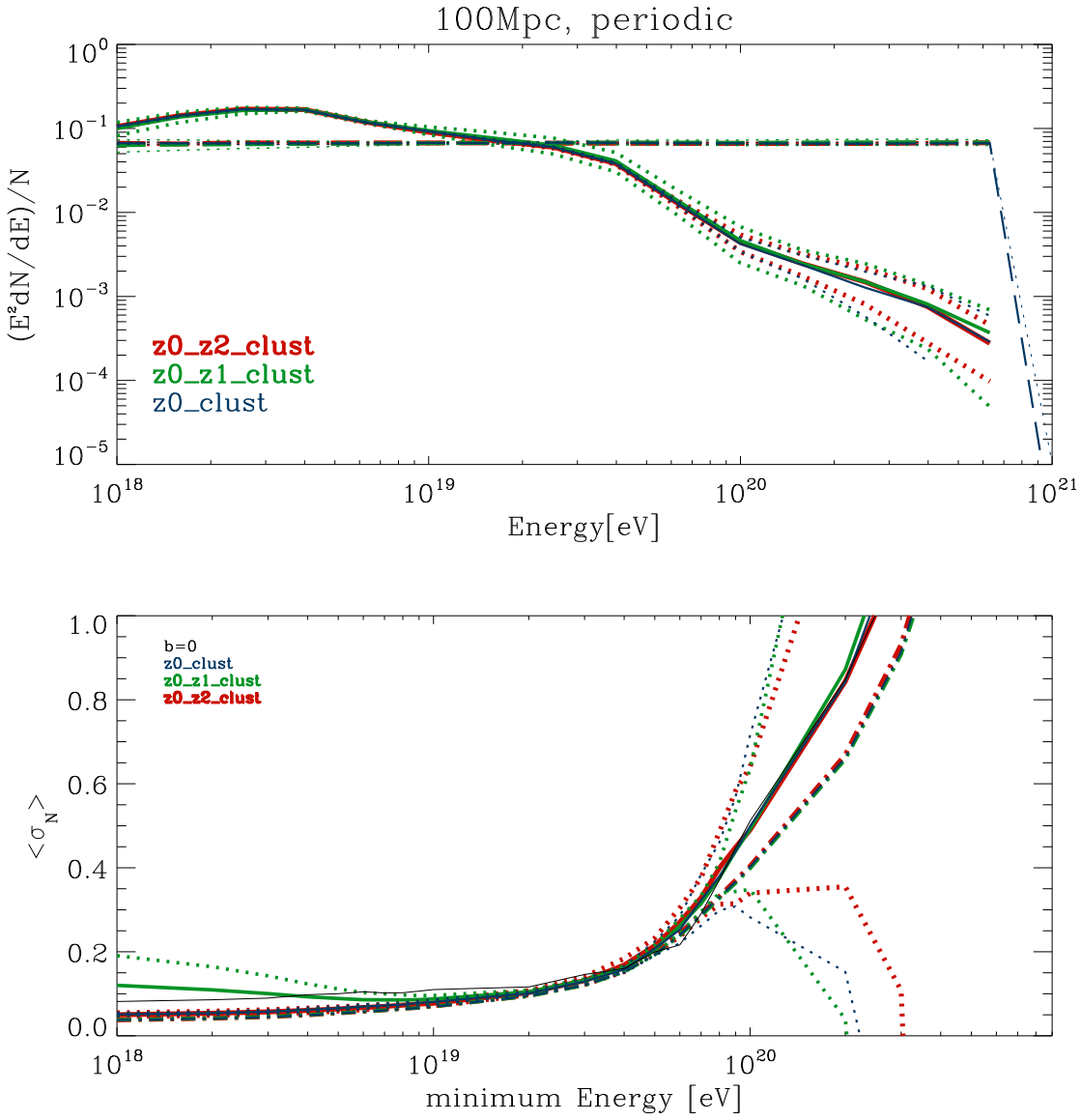

Figure 5.6: Spectrum (top) and anisotropic variance σ_N (bottom) of the different seeding models of the 100Mpc simulations without (*z0*) and with additional magnetic seeding at $z \sim 1$ (*z0_z1*) and $z \sim 2$ (*z0_z2*) for random injection. This figure shows the average of 10 clusters for 10^6 injected UHECRs. The dashed line shows the injected spectrum, the solid line the arrival spectrum. The dotted lines show the corresponding 2σ standard deviation. The dash dotted lines show the mean Poissonian shot noise. The *b=0* case is a single random injection run without magnetic fields for comparison.

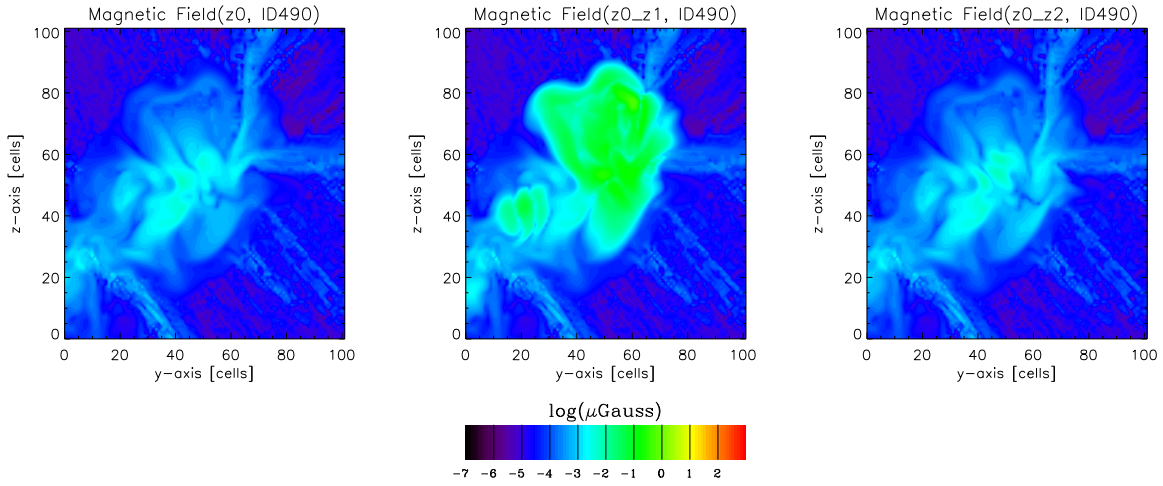

Figure 5.7: Contour maps of magnetic field of Cluster ID490 of the 100 Mpc simulation without (*z0*) and with additional magnetic seeding at $z \sim 1$ (*z0_z1*) and $z \sim 2$ (*z0_z2*) at z=0, the side of each panel is 20 Mpc, the slice is one cell ($\sim$ 200 kpc) thick

Summary 5.2:

- We find that the different seeding models of magnetic fields do not show any differences neither for the arrival spectrum nor for the anisotropy of the UHECRs, because these do not undergo too strong deflections in CMFs.
- This is robust also against the increase of number statistics of high energy events.
- This stems likely from the fact that all different investigated seeding models do not produce significant differences at the scale of filaments, i. e. for $B \lesssim 10^{-3}\mu$G.
- At low energies ($E < 10^{19}$ eV) our runs suggest that a detectable difference of $z \sim 1$ seeding is adopted, at a level $> 2\sigma$ respect to the Poissonian noise. This effect accounts for $\sim 10\%$ anisotropy and it is in principle in a range that observations can explore.

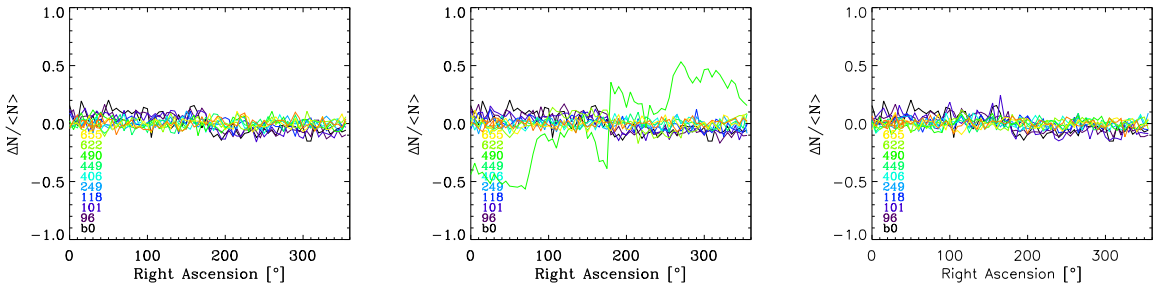

Figure 5.8: Anisotropy profiles of arriving UHECRs of the 5 different clusters in 100 Mpc simulations without (*z0*) and with additional seeding at $z \sim 1$ (*z0_z1*) and $z \sim 2$ (*z0_z2*). Shown is the variation of number of particles arriving within 5° of right ascension. In each panel we also show the anisotropy for one observer in the $b = 0$ model, that by definition gives the level of the Poissonian shot noise in the runs.

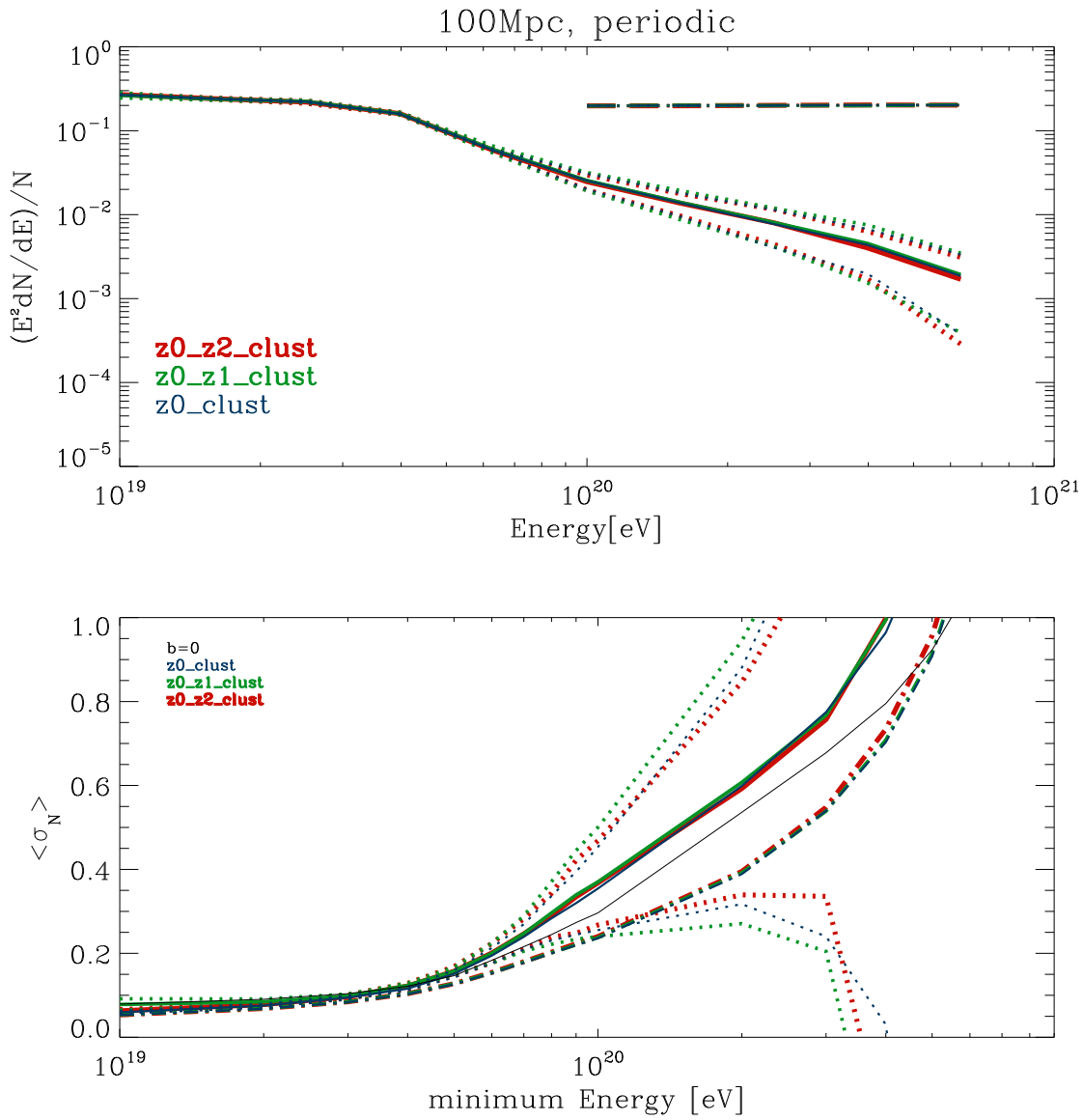

Figure 5.9: Spectrum (top) and anisotropic variance σ_N (bottom) of the different seeding models of the 100 Mpc simulations without (*z0*) and with additional seeding at $z \sim 1$ (*z0_z1*) and $z \sim 2$ (*z0_z2*) for random injection. This figure shows the average of 10 clusters for 10^6 injected UHECRs where the energy range of injection is limited to the range of 10^{20} to 10^{21} eV and only UHECRs with arrival energy above 10^{19} eV are considered. The dashed line shows the injected spectrum, the solid line the arrival spectrum. The dotted lines show the corresponding 2σ standard deviation. The dash dotted lines show the mean Poissonian shot noise. The *b=0* case is a single random injection run without magnetic fields for comparison.

6. Conclusion

Our study investigated the influence of magnetic field seeding scenarios and location of injection source positions on the energy spectrum of UHECRs and on their anisotropic distribution seen by mock observers. We did so by comparing the energy spectrum and the anisotropic variance of CRPropa calculations with random as well as with cluster source injection using simulations with different seeding scenarios. The simulations employed both, simple uniform seeding of primordial magnetic fields ($B = 10^{-4}\mu$G at $z \sim 30$) and additional efficient seeding from cluster halos at $z \sim 1$ or $z \sim 2$ (see 4.1).

First, we analyzed the magnetic field simulations and found that the additional magnetic field seeding first strengthens the magnetic field on the density peaks and releases thereafter into larger volumes around clusters (Sec. 4.2).
We then examined the functional parameters of CRPropa to find a suitable set of parameters that save computation time but do not lose any physical information for the further investigation. (Sec. 4.3).

The main focus of our thesis was devoted at examining the influence of the magnetic field seeding model and of the location of injection of sources of UHECRs on the spectra of arrival direction and on the anisotropic variance (Sec. 5.1 – 5.2).

- The injection of UHECRs from clusters can be distinguished from random isotropic injection for $E > 10^{20}$ eV events, as the arrival spectrum is higher by a factor of ~ 2.
- Above the GZK limit ($5 \cdot 10^{19}$ eV) in case of random isotropic injection the anisotropy of UHECRs is consistent with the Poissonian noise statistics, while in case of cluster injection it is significantly larger (a $1-2\sigma$ level).
- At high energies the different seeding models of magnetic fields do not show any differences, neither for the arrival spectrum nor for the anisotropy of the UHECRs. This stems likely from the fact that all different investigated seeding models do not produce significant differences at the scale of filaments, i. e. for $B \lesssim 10^{-3}\mu$G.
- At low energies ($E < 10^{19}$ eV) our runs suggest that a detectable difference for additional seeding at low redshift ($z \sim 1$) is adopted, at a level $> 2\sigma$ respect to the Poissonian noise. This effect accounts for $\sim 10\%$ anisotropy and it is in principle in a range that observations can explore.

We briefly comment about the observational implications of our results, even if we notice that the assumption made so far (pure proton composition of the injected UHECRs, for the sake of simplicity) limits its quantitative comparison with real data. The significant difference we measured between the spectra and the anisotropy distribution obtained with isotropic and cluster-based injection of UHECRs is at a potentially observable level, since at the relevant

energies here ($E \sim 10^{20} - 10^{21}$eV) the deflection of particles by the magnetic field in the Milky Way should be negligible (i. e. from Eq. 2.2 it follows that the Larmor radius at these energies is $\gg$ than the size of the Milky Way, and therefore the most important deflections can be only due to the extragalactic field). Conversely, the difference we measure at low energies, $E < 10^{19}$eV, between different seeding models are potentially more difficult to observe, even if they are significant compared to Poissonian noise there, as at these energies the Larmor radius of particles is smaller than the radius of the Milky Way ($r_L \leq 1 - 10$kpc) and the scatter and diffusion of UHECRs within the Milky Way becomes dominant (e. g. *Farrar* 2012 [**36**]).

Whether or not the residual extragalactic signal can be detected and used to constrain models for the seeding of magnetism in large-scale structures, it is a very crucial point in the current study of UHECRs. Establishing whether the intensity of extragalactic UHECRs dominate the cosmic ray spectrum above 10^{18}eV and if the transition from galactic to extragalactic cosmic rays should leave a signature in energy-dependent anisotropy at EeV energy or below, would represent a major step forward in the theory (e. g. *Deligny* 2012 [**35**]).

In future development on this topic it would be helpful to further investigate the dependency of arrival spectrum and anisotropy on the location of sources of UHECRs, with increased statistics of events above 10^{20} eV, to distinguish the outcome more precisely. It would also be beneficial to explore differences as a function of the minimum density of source locations of UHECRs to draw conclusions on their origin.

Another advantage would be to compare more magnetic field seeding models to find ways to identify the origin of CMF using UHECR measurements. In principle, lower energies should be treated preferential to investigate magnetic field seeding models with the use of CRs.

In general, a better resolution as well as a smaller observer sphere in the CRPropa runs would lead to more realistic data. Furthermore, the composition of injected particles should be extended to consider more effects present during propagation, like photo-disintegration and nuclear decay.
To allow the direct application to real observational data it would also be useful to produce all-sky maps of events and decomposition of the observation of UHECRs into spherical harmonics.

7. Acknowledgement

First, I would like to thank Prof. Marcus Brüggen for providing me with the very interesting topic of this thesis. Furthermore I would like to thank my dedicated supervisor Dr. Franco Vazza for his unstinting support throughout the whole thesis. Finally, my thanks go to my family and to Nadine for private support .

Additionally the whole group would like to thank Prof. G. Sigl and R. Alves Batista for their precious scientific support, as well as all the other developers of CRPropa for making the code publicly available.

We also acknowledge the usage of computational resources of the CHRONOS Call 2014 at CSCS (Lugano, Switzerland) and at the Julich Supercomputing Center (JSC) under project number 7006, as well as the use of resources of the Golem Cluster at Hamburger Sternwarte.

References

[1] J. R. Hörandel, Early Cosmic-Ray Work Published in German
arXiv:1212.0706v1 [physics.hist-ph] 4 Dec 2012

[2] W. F. Hanlon, Cosmic Ray Spectra of Various Experiments
`http://www.physics.utah.edu/~whanlon/spectrum.html` Aug 2014

[3] A. Letessier-Selvon, Highlights from the Pierre Auger Observatory
arXiv:1310.4620v2 [astro-ph.HE] 19 Oct 2013

[4] P. Auger, R. Maze, T. Grivet-Meyer, Academie des Sciences **206**, 1721 (1938);
P. Auger, R. Maze, ibid. **207**, 228 (1938)

[5] M. Unger *et al.*, Mass Composition Working Group Report at UHECR-2012
arXiv:1306.4430 [astro-ph.HE] 19 Jun 2013

[6] E. M. Santos *et al.*, Anisotropy Studies with the Pierre Auger Observatory
arXiv:0902.0040v1 [astro-ph.HE] 31 Jan 2009

[7] P. Necesal, The Fluorescence Detector of the Pierre Auger Observatory
arXiv:1011.6523v1 [astro-ph.IM] 30 Nov 2010

[8] F. Salamida *et al.*, The exposure of the hybrid detector of the Pierre Auger Observatory
arXiv:1010.6162v1 [astro-ph.HE] 29 Oct 2010

[9] G. Sigl, Ultra-High Energy Cosmic Rays: A Probe of Physics and Astrophysics at Extreme Energies
arXiv:astro-ph/010429117 Apr 2001

[10] H. Takami, Propagation of Ultra-High-Energy Cosmic Rays
SLAC eConf, C111215 22. Jun 2012

[11] A. A. Watson, High-Energy Cosmic Rays and the Greisen-Zatsepin-Kuzmin Effect
arXiv:1310.0325 [astro-ph.HE] 1. Oct 2013

[12] K. Greisen, End of the cosmic ray spectrum?
Phys. Rev. Lett.16, 748 (1966)

[13] G. T. Zatsepin and V. A. Kuz'min, Upper Limit of the Spectrum of Cosmic Rays
JETP Lett. 4, 78 (1966)

[14] M. Brüggen, Magnetic fields in galaxy clusters
Astronomische Nachrichten / **AN 334**, No. 6, 543 547 (2013), doi 10.1002/asna.201311895

[15] A. Bonafede *et al.*, A non-ideal MHD Gadget: Simulating massive galaxy clusters
arXiv:1107.0968v1 [astro-ph.CO] 5 Jul 2011

[16] L. M. WIdrow *et al.*, The First Magnetic Fields
arXiv:1109.4052 [astro-ph.CO] 19 Sep 2011

[17] S. Bertone *et al.*, Magnetic Field Seeding by Galactic Winds
arXiv:astro-ph/0604462v1 21 Apr 2006

[18] J. Donnert *et al.*, Cluster Magnetic Fields from Galactic Outflows
arxiv:0808:0919v2 [astro-ph] 28 Oct 2008

[19] R. E. Pudritz *et al.*, Magnetic Fields in Astrophysical Jets: From Launch to Termination
arxiv:1205.2073v2 [astro-ph.HE] 24 may 2012

[20] A. Bonafede *et al.*, The Coma cluster magnetic field from Faraday rotation measures
arXiv:1002.0594v1 [astro-ph.CO] 2 Feb 2010

[21] V. L. Ginzuburg & S. I. Syrovatskii, Cosmic Magnetobremsstrahlung (Synchrotron Radiation)
Annual Review of Astronomy and Astrophysics Vol. 3: 297-350 (Volume publication date September 1965) doi: 10.1146/annurev.aa.03.090165.001501

[22] R. Beck, Measuring interstellar magnetic fields by radio synchrotron emission arXiv:0812.4925 [astro-ph] 29 Dec 2008

[23] G. L. Bryan *et al.*, Enzo: An Adaptive Mesh Refinement Code for Astrophysics arXiv:1307.2265v1 [astro-ph.IM] 8 Jul 2013;
http://enzo-project.org

[24] A. Dedner *et al.*, Hyperbolic Divergence Cleaning for the MHD Equations Journal of Computational Physics **175**, 645673 (2002), doi:10.1006/jcph.2001.6961, 2002

[25] A. Kurganov & E. Tadmor, New High-Resolution Central Schemes for Nonlinear Conservation Laws and ConvectionDiffusion Equations Journal of Computational Physics **160**, 241282 (2000), doi:10.1006/jcph.2000.6459

[26] C.-W. Shu & S. Osher, Efficient implementation of essentially non-oscillatory shock-capturing schemes Journal of Computational Physics **77**, 439471 (1988), doi: 10.1016/0021-9991(88)90177-5

[27] T. Abel, P. Wang *et al.*, Lowering the Characteristic Mass of Cluster Stars by Magnetic Fields and Outflow Feedback arXiv:1008.0409v1 [astro-ph.SR] 2 Aug 2010

[28] E. Komatsu *et al.*, Seven-Year Wilkinson Microwave Anisotropy Probe (WMAP) Observations: Cosmological Interpretation arXiv:1001.4538v3 [astro-ph.CO] 9 Nov 2010

[29] Exelis Visual Information Solutions, *IDL Software* . (http://www.exelisvis.com/ProductsServices/IDL.aspx , Aug 2014)

[30] E. Armenaud & G. Sigl *et al.*, CRPropa: A Numerical Tool for the Propagation of UHE Cosmic Rays, rays and Neutrinos arXiv:astro-ph/0603675v2 18 Nov 2007

[31] G. Sigl *et al.*, CRPropa 2.0 a Public Framework for Propagating High Energy Nuclei, Secondary Gamma Rays and Neutrinos arXiv:1206.3132v1 [astro-ph.IM] 14 Jun 2012

[32] R. Alves Batista *et al.*, CRPropa 3.0 a Public Framework for Propagating UHE Cosmic Rays through Galactic and Extragalactic Space arxiv:1307.2643v1 [astro-ph.IM] 10 Jul 2013

[33] A. Mücke *et al.*, Computational Physics Community **124**, 290 (2000)

[34] P. Sommers, Cosmic Ray Anisotropy Analysis with a Full-Sky Observatory arXiv:astro-ph/0004016v1 3 Apr 2000

[35] O. Deligny, Review of the Anisotropy Working Group at UHECR-2012 arXiv:1306.4998v1 [astro-ph.HE] 20 Jun 2013

[36] Farrar, Galactic magnetic deflections and Centaurus A as a UHECR source arXiv:1211.7086v1 [astro-ph.HE] 29 Nov 2012

List of Figures

A. Appendix

The most important examples of the original IDL codes developed for this thesis are given in the following. All codes were designed to analyze directly the output of CRPropa, which is plain text and can be read out via `READCOL` procedure, or the output of *ENZO*'s simulations, which are in HDF5 format (an example to read out this data is given in A.1).

In general, the main code is given a simulation together with a corresponding catalog of clusters and the parameters of the CRPropa runs to be considered. It reads the information about the clusters out of the catalog and finds all the necessary CRPropa runs and calls the wanted function, with all these runs one after another.
Though the programming required to plot the graphs was a considerable part of the thesis, these routines are not explained in detail as they do not hold much significant information for the reader. We will only give a list of the used functions (see *IDL* [**29**] for more detail):

ARROWS CONTOURS (O)PLOT XYOUTS

A.1. read_density.pro

```
FUNCTION read_density,
        simulation      ;... simulation to read out (hdf5 format)

cd=6.8e-29 ;...g/cm^3           ;... cosmic mean density
                                ;(to correct data units)

  ido=h5f_open(file)            ;... readout hdf5 file
   itemp=h5d_open(ido,'density')
   datasp=h5d_get_space(itemp)
   density = H5D_READ(itemp)
   h5d_close,itemp

density*=cd                     ;... correct units
RETURN, density
END
```

A.2. profile.pro

lat

```
FUNCTION profile,
        data,           ;... 3D data array from simulation
        max,            ;... radius to take profile in
        xc, yc, zc,     ;... coordinates of the cluster center


s=SIZE(data)
s=s(1)
prof=FLTARR(max,2)      ;... create temporary profile array with extra
prof(*)=0.              ;    dimension to count cells, set to zero

FOR l=0,2*max-1 DO BEGIN        ;... loop in the 3 directions
 FOR j=0,2*max-1 DO BEGIN
  FOR i=0,2*max-1 DO BEGIN
   x=i+xc-nr            ;... translate the coordinates from the
   y=j+yc-nr            ;    reference frame of the cluster into
   z=l+zc-nr            ;    the ref.frame of the simulation
  ;... compute distance from center to current cell
   radius=SQRT((i-max)^2.+(j-max)^2.+(l-max)^2.)
  IF radius LE 2*max THEN BEGIN
   IF x LT 0    THEN x=s-x      ;... if coordinates exceed simulation
   IF y LT 0    THEN y=s-y      ;    box, use periodicity of it and
   IF z LT 0    THEN z=s-z      ;    take values from other side of
   IF x GE s    THEN x-=s       ;    the box instead
   IF y GE s    THEN y-=s
   IF z GE s    THEN z-=s
   prof(radius,0)+=data(x,y,z)    ;... build the total value and
   prof(radius,1)+=1              ;... count the number of cells in
  ENDIF                           ;    each spherical shell
  ENDFOR
 ENDFOR
ENDFOR

profile=FLTARR(SIZE(prof))              ;... create target array and
profile(*)=prof(*,0)/FLOAT(prof(*,1))   ;... build the profile of the
RETURN,profile                        ; average field value (total/#cell)
END
```

A.3. average_spectrum.pro

```
FUNCTION average_spectrum,
        catalog,                ;... catalog of clusters and
        CRPropa_run             ;    array with CRPropa output filenames
                                ;    of a given simulation
;... constants for spectrum
mine=1e18                       ;... minimum energy (eV)
maxe=1e21                       ;... maximum energy (eV)
bine=0.2                        ;... log(energy) binsize for histogram
nbins=UINT((maxe-mine)/bine)+1  ;... number of bins
   ;... read clusters position and parameters from catalog (plain text)
 READCOL, catalog, $
        id, xc, yc, zc, r, mass, temp, bmean, bmax
nn=SIZE(id)
ncluster=nn(1)                  ;... get number of clusters
spectrum0 = FLTARR(ncluster,nbins)      ;... prepare temporary arrays
spectrum1 = FLTARR(ncluster,nbins)
spectrum_plot = FLTARR(2,nbins,4)

FOR cluster=0,ncluster-1 DO BEGIN       ;... for every cluster
  READCOL,CRPropa_run[cluster], $       ;... read CRPropa output
        d,ids,id0,e,e0,x,y,z,x0,y0,z0,px,py,pz,p0x,p0y,p0z,zed
 e0=alog10(e0)+18               ;... injection and
 e=alog10(e)+18                 ;    arrival energies in log(eV)
        ;... compute initial spectrum of CR
 spec0=histogram(e0,min=mine,max=maxe,binsize=bine)
        ;    and final spectrum of CR received at observer
 spec1=histogram(e,min=mine,max=maxe,binsize=bine)
 spectrum0[cluster,*]=FLOAT(spec0) ;... convert spectra to float and
 spectrum1[cluster,*]=FLOAT(spec1) ;    fill into the temporary arrays
ENDFOR
FOR bin=0,nbins-1 DO BEGIN ;... for every bin
    ;... compute the average value together with the standard deviation
 spectrum_plot[0,bin,*]  = MOMENT(spectrum0[*,bin]) ; for initial
 spectrum_plot[1,bin,*]  = MOMENT(spectrum1[*,bin]) ; and final spectrum
ENDFOR
RETURN, spectrum_plot
END
```

A.4. anisotropy_profile.pro

```
FUNCTION anisotropy_profiler,
        CRPropa_run,     ;... CRPropa outputfile (.dat)
        xc, yc, zc,      ;... coordinates of the cluster center
        elimit           ;... energy limit of events taken into account

angle = 5 ; degrees      ;... resolution for sectors in right ascension
profile = FLTARR(360/angle) ;... create target array for profile
;(shot_noise = profile  ;... and for shot noise)
READCOL,CRPropa_run, d,idcr,id0,e,e0,x,y,z, ... ;... read crpropa data

        ;... compute right ascension of arrival position

tanyx = ATAN((y-yc[c])/(x-xc[c]))/!DTOR+90

FOR phi=0,180-angle,angle DO BEGIN       ;... for every sector

 ixplus  = WHERE( tanyx GE phi AND tanyx LT phi+angle $
           AND    z-zc[c] GE 0 $         ;... in one hemisphere
           AND    e GE elimit, $  ; (above minimum considered energy)
                  countplus)
 ixminus = WHERE( tanyx GE phi AND tanyx LT phi+angle $
           AND    z-zc[c] LT 0 $         ;... and in the opposite one
           AND    e GE elimit, $
                  countminus)
 profile[phi/angle] = countplus          ;... count the arrivals
 profile[(phi+180)/angle] = countminus
;( shot_noise[elim]+= countplus+countminus      ;... additional for shot
    noise
; shot_noise[elim]*=5./360.           ;... as an average of all sectors)
ENDFOR

        ;... compute the relative variance to be the profile

profile = FLOAT(profile-MEAN(profile))/MEAN(profile)
RETURN, profile ;(, shot_noise)
END
```

A.5. sigma.pro

```
FUNCTION sigma,
        CRPropa_run,     ;... CRPropa outputfile (.dat)
        xc, yc, zc,      ;... coordinates of the cluster center

        ;... prepare values for x-coordinates

elimit_mag=[0,3]         ;... magnitudes of energy limits in EeV
elimit=FLTARR(9*(mag[1]-mag[0]))
FOR i=elimit_mag[0],elimit_mag[1]-1 DO BEGIN
;... combine every order of magnitude with all digits
 FOR j=0,8 DO elimit[(i-mag[0])*9+j] = (j+1)*10^i
ENDFOR
nelimit = SIZE(elimit)
nelimit = nelimit[1]     ;... get number of energy limits

        ;... calculate anisotropic variance

sigma = FLTARR(nelimit,4);... create target array
FOR elim=0, nelimit-2 DO BEGIN  ;... for every energy limit
;.. calculate the average relative variance and it's standard deviation
 sigma[elim,*] = MOMENT(ANISOTROPY_PROFILE(CRPropa_run, xc,yc,zc, elim))
ENDFOR

shot_noise=SQRT(shot_noise)/shot_noise ;... calculate shot noise

RETURN, sigma ;(,shot_noise)
END
```

The average value and standard deviation of several `sigma` outputs were computed by use of the `MOMENT` function.

Hiermit bestätige ich, dass die vorliegende Arbeit von mir selbständig verfasst wurde und ich keine anderen als die angegebenen Hilfsmittel insbesondere keine im Quellenverzeichnis nicht benannten Internet-Quellen benutzt habe und die Arbeit von mir vorher nicht einem anderen Prüfungsverfahren eingereicht wurde. Die eingereichte schriftliche Fassung entspricht der auf dem elektronischen Speichermedium. Ich bin damit einverstanden, dass die Bachelorarbeit veröffentlicht wird.

Hamburg, den 22. September 2014,